

# Quadrature by fundamental solutions: kernel-independent layer potential evaluation for large collections of simple objects

David B. Stein · Alex H. Barnett

the date of receipt and acceptance should be inserted later

**Abstract** Well-conditioned boundary integral methods for the solution of elliptic boundary value problems (BVPs) are powerful tools for static and dynamic physical simulations. When there are many close-to-touching boundaries (eg, in complex fluids) or when the solution is needed in the bulk, nearly-singular integrals must be evaluated at many targets. We show that precomputing a linear map from surface density to an *effective source* representation renders this task highly efficient, in the common case where each object is “simple”, ie, its smooth boundary needs only moderately many nodes. We present a kernel-independent method needing only an *upsampled smooth* surface quadrature, and one dense factorization, for each distinct shape. No (near-)singular quadrature rules are needed. The resulting effective sources are drop-in compatible with fast algorithms, with no local corrections nor bookkeeping. Our extensive numerical tests include 2D FMM-based Helmholtz and Stokes BVPs with up to 1000 objects (281000 unknowns), and a 3D Laplace BVP with 10 ellipsoids separated by 1/30 of a diameter. We include a rigorous analysis for analytic data in 2D and 3D.

**Keywords** Boundary integral equations · Singular quadrature · Near-singular quadrature · Nyström · method of fundamental solutions · Fluid dynamics

**Mathematics Subject Classification (2000)** 45A05 · 35C15 · 35J25 · 76S05

## 1 Introduction

Boundary integral equations (BIEs) are advantageous for the numerical solution of a wide variety of linear boundary-value problems (BVPs) in science and engineering [59, 46]. They include electro/magnetostatics [35, 102], acoustics [82, 58], electromagnetics/optics [19, 18, 64], elastostatics/dynamics [42, 16], viscous fluid flow [100, 78, 88, 74, 73], electrohydrodynamics [89], and many others. BIEs also form a component in

---

David B. Stein

Center for Computational Biology, Flatiron Institute, New York, NY 10010, USA E-mail: dstein@flatironinstitute.org

Alex H. Barnett

Center for Computational Mathematics, Flatiron Institute, New York, NY 10010, USA

solvers for BVPs with volume driving and/or nonlinearities by solving for a homogeneous PDE solution which corrects the boundary conditions [71, 11, 27, 26, 1, 103]. “Fast” (quasi-linear scaling) algorithms to apply the resulting discretized operators, such as the fast multipole method (FMM) [37, 17, 18], have revolutionized the size of problems that can be tackled [69]. More recently, fast direct solvers have enabled large gains when iterative solution is inefficient [38, 70, 29]. Despite this progress, the issue of efficient and accurate discretization of BIEs in complex geometries persists. In this work we present a new tool to address this in the common case of a large number of simple, possibly close-to-touching objects, as can arise in numerical homogenization, porous media, and complex fluids.

For example, and to fix notation, let  $\Omega$  be either one bounded obstacle or the union of many such obstacles in  $\mathbb{R}^d$ , let  $L$  be a linear constant-coefficient 2nd-order elliptic differential operator, and consider solving the BVP

$$\mathcal{L}u = 0 \quad \text{in } \mathbb{R}^d \setminus \overline{\Omega} \quad (1)$$

$$u = f \quad \text{on } \partial\Omega \quad (2)$$

with an appropriate decay or radiation condition imposed on  $u(\mathbf{x})$  as  $\|\mathbf{x}\| \rightarrow \infty$ . In terms of the translationally invariant fundamental solution (free space Green’s function) for  $\mathcal{L}$ , denoted by  $G(\mathbf{x}, \mathbf{y}) = G(\mathbf{x} - \mathbf{y})$ , for  $\mathbf{x}, \mathbf{y} \in \mathbb{R}^d$ , a common *layer potential* representation for the solution is, in the scalar case,

$$u(\mathbf{x}) = [(\alpha\mathcal{S} + \beta\mathcal{D})\tau](\mathbf{x}) := \int_{\partial\Omega} \left( \alpha G(\mathbf{x}, \mathbf{y}) + \beta \frac{\partial G(\mathbf{x}, \mathbf{y})}{\partial \mathbf{n}_{\mathbf{y}}} \right) \tau(\mathbf{y}) ds_{\mathbf{y}}, \quad \mathbf{x} \in \mathbb{R}^d \setminus \overline{\Omega}. \quad (3)$$

Here  $ds_{\mathbf{y}}$  is the arc or surface element,  $\mathbf{n}_{\mathbf{y}}$  the unit outward normal at  $\mathbf{y} \in \partial\Omega$ , and the formula defines the single-layer  $\mathcal{S}$ , and (again in the scalar case only) double-layer  $\mathcal{D}$  potentials. The constants  $\alpha$  and  $\beta$  are given. The unknown *density* function  $\tau$  lives on  $\partial\Omega$  and is found by solving a so-called *indirect* BIE derived from (3) by taking the exterior limit  $\mathbf{x} \rightarrow \partial\Omega$ , using jump relations [46, 19]. In the case of Dirichlet boundary conditions, this BIE is

$$[\alpha\mathcal{S} + \beta(\tfrac{1}{2}I + D)]\tau = f, \quad (4)$$

where  $f$  is given boundary data, and  $S$  and  $D$  are the principal value *boundary integral operators* resulting by restricting  $\mathcal{S}$  and  $\mathcal{D}$  to  $\partial\Omega$ . Note that, since (at least for  $\partial\Omega$  smooth)  $S$  and  $D$  are compact, for  $\beta \neq 0$  the BIE is of Fredholm 2nd-kind; in general  $\alpha$  and  $\beta$  are chosen to give this property and to give a unique solution [46, 5].

Despite this elegant framework, in practice there remain two challenging tasks:

1. high-order accurate discretization of (4), meaning filling (or, for large problems, merely applying) the  $N \times N$  Nyström matrix in a linear system

$$A\tau = \mathbf{f}, \quad (5)$$

which approximates (4); and

2. numerical evaluation of (3) at target points  $\mathbf{x}$  including those arbitrarily close to  $\partial\Omega$ , given the solution  $\tau \in \mathbb{C}^N$  to (5).

Much of the difficulty of both tasks originates in the *singularity* in  $G(\mathbf{x} - \mathbf{y})$  as  $\mathbf{x} \rightarrow \mathbf{y}$ . Their troublesome nature for various kernels, especially in 3D ( $d = 3$ ) and/or complex geometries, is indicated by the large number of methods, and its active growth as a research area (briefly reviewed in Section 1.1).

Task 2 arises especially frequently in fluid simulations containing many interacting bodies, e.g. in blood and vesicular flow or sedimentation problems. For either rigid or deformable particles BIE solutions (or simpler hydrodynamic layer-potential evaluations [94]) are typically needed at every time-step, and regularizations [88] or special near-field quadrature schemes must be used to maintain fidelity (see Section 1.1). When non-Newtonian rheology arises, as in complex and active fluids, continuum models typically track extra stress or orientation fields [84] in the bulk whose evolution requires knowledge of both hydrodynamic velocities and stresses. Due to the difficulty of BIEs, simulations of such complex fluid and active matter systems have instead primarily been done using finite/spectral element methods and cut cell methods in stationary geometries [75, 92], and regularized methods [22, 77, 66] in moving geometries. In certain cases such regularized methods are known to give inaccurate results, with nontrivial corrections required to ensure convergence [60, 91]. Thus robust methods for BIE with many near-boundary targets can enable complex fluid simulations in regimes that are currently hard to access.

In many applications the number of nodes needed on each distinct boundary is “small” (at most a few thousand, in either 2D or 3D). In this case dense, linear algebraic methods with  $\mathcal{O}(N^3)$  cost are practical for per-object precomputations. This handles the diagonal (self-interaction) blocks of  $A$ ; an FMM, followed by local corrections, may then apply its off-diagonal blocks. Focusing on Nyström discretizations [59, Ch. 12] [19] for indirect BIEs, we exploit this idea to propose a simple but efficient new approach to both tasks 1 and 2, that is in large part kernel- and dimension-independent, and furthermore is already in use [103]. Its kernel-independence allows easy switching between PDEs, or to axisymmetric, periodic, or multilayer Green’s functions. It is essentially automated in 2D, but requires parameter adjustment in 3D. A key advantage at the implementation level is that a *single* FMM-compatible representation covers on-surface, near-surface, and far-field, bypassing the bookkeeping that complicates high-performance codes [100].

Let us sketch the basic proposal in a simple 2D exterior acoustic frequency-domain scattering (Helmholtz) Dirichlet BVP, with a single boundary curve  $\partial\Omega$ ; see Fig. 1. The incident plane wave has wavenumber  $k$ , and the resulting scattered wave  $u$  solves the BVP with data the negative of this incident wave on  $\partial\Omega$ . This ensures that their sum (the physical solution shown in panel (a)) has zero Dirichlet boundary data. In the representation (3),  $\alpha = -ik$ ,  $\beta = 1$  (the usual “combined field” or CFIE [19]), and  $G(\mathbf{r}) = (i/4)H_0^{(1)}(k\|\mathbf{r}\|)$ , where  $H_0^{(1)}$  is the Hankel function of the first kind. Panel (b) shows the plain  $N$ -node periodic trapezoid rule (PTR) quadrature used on  $\partial\Omega$ .

The main idea—which we call quadrature by fundamental solutions (QFS)—is to place roughly  $N$  effective or proxy sources a controlled distance from  $\partial\Omega$  on its *non-physical* (interior) side, whose strengths are chosen to approximate the desired potential (3), both on  $\partial\Omega$  and throughout the solution domain  $\mathbb{R}^d \setminus \overline{\Omega}$ . We precompute a “source-from-density” matrix  $X$  mapping any smooth boundary density sample vector  $\boldsymbol{\tau}$  to an equivalent proxy strength vector. This matrix equation for  $X$  is solved densely in a backward-stable fashion by *collocation* (matching) of the potential, either on the surface  $\partial\Omega$  (as in panel (c)), or on a nearby set of “check points” a controlled distance from  $\partial\Omega$  but on the *physical* side (panel (d)). Armed with  $X$ , given any density  $\boldsymbol{\tau}$  the desired potential (3) is well approximated by a sum over the proxy sources with strengths  $\boldsymbol{\sigma} = X\boldsymbol{\tau}$ . This applies for targets  $\mathbf{x}$  far from  $\partial\Omega$ , arbitrarily near to  $\partial\Omega$ , or on  $\partial\Omega$  (the exterior surface limit), and is compatible with the FMM. This addresses

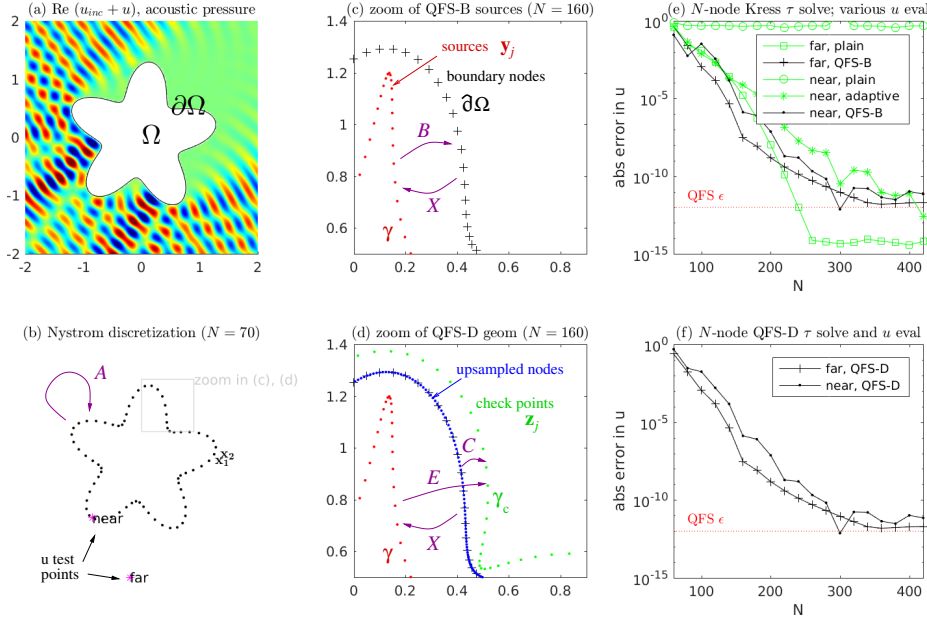


Fig. 1: Overview of proposal applied to an exterior Dirichlet Helmholtz (sound-hard) scattering BVP from  $\partial\Omega$  parameterized in polars by  $r(t) = 1 + 0.3 \cos(5t + 0.2)$ , that is,  $\mathbf{x}(t) = (r(t) \cos t, r(t) \sin t)$ . (a) Incident wave (from bottom left at  $\theta = \pi/5$ , wavenumber  $k = 20$ ) plus scattered wave (BVP solution  $u$ ). (b) Discretization nodes (indicating action of Nyström matrix  $A$ ), and “far” and “near” test targets. (c) QFS-B proxy sources (red dots) and boundary nodes (+ symbols) (d) QFS-D proxy sources (red dots), check points (green dots), and upsampled boundary nodes (blue dots). (e) Errors in  $u$  for various evaluation methods, having solved the density vector using Kress quadrature for  $A$ . (f) The full “desingularized” scheme: errors in  $u$ , having first solved the density using  $A$  as filled via QFS-D. Note that the black curves converge at comparable rates to the green ones down to the requested tolerance  $\epsilon$ .

task 2 above. Furthermore, by filling the evaluation matrix  $B$  (see panel (c)) from proxy sources to the desired data type (trace) on  $\partial\Omega$ , then the product  $BX$  is a good approximation to  $A$ , the Nyström matrix in (5), completing task 1.

In Fig. 1(e) we show convergence of potential evaluation (task 2) for two target points (plotted in panel (b)), given a density  $\tau$  already solved using the Kress scheme [58] generally considered a “gold standard” [39, 43]. For the easy case of a far target, our QFS proposal has a similar convergence rate as the plain PTR, down to the requested tolerance of  $\epsilon = 10^{-12}$ . For a near target (a distance  $10^{-4}$  from  $\partial\Omega$ , where the plain PTR of course fails dismally), the same QFS scheme has similar convergence to the expensive gold-standard method of adaptive Gaussian quadrature applied to the trigonometric polynomial interpolant of the density, again down to  $\epsilon$ . In Fig. 1(f) we use QFS both to fill the Nyström matrix  $A$  and for potential evaluation (combining tasks 1 and 2); again we see similar convergence.

**Remark 1 (MFS)** *The idea of representing homogeneous PDE solutions by Green’s function sources near the boundary has a 50-year history in the engineering community*



[61, 25], being called the method of fundamental solutions [12, 7, 67], method of auxiliary sources [87], charge simulation method [53, 55], 1st-kind integral equations [49, 50, 33], rational approximation [45, 34], etc. It is well known to produce exponentially ill-conditioned linear systems. Recently, similar “proxy point” ideas flourished in fast direct solvers [70], kernel-independent FMMs [69], and BIE quadrature [81]. Our novelty here is to use off-surface collocation to make a black-box general layer-potential evaluator tool, which can be inserted, for example, into standard well-conditioned 2nd-kind BIE frameworks.

The method’s simplicity and MFS flavor restricts the body shapes to which it may be accurately applied. This arises essentially from the need that the density  $\tau$  and data  $f$  be smooth on the local node-spacing scale  $h$ . Yet, this is also true for (non-adaptive) BIE quadrature schemes generally. If smooth objects become extremely close ( $\mathcal{O}(h^2)$  or closer), *adaptive* surface quadratures are essential to capture  $\tau$  [41, 99, 72], a problem beyond even tasks 1 and 2. We will not address adaptivity, since many BIE applications use hand-tuned non-adaptive quadratures. We target simulations involving simple bodies, but a large number of them, hence we test only global quadratures, leaving panel quadratures for the future. We note that the MFS can also handle 2D corner domains using a moderate number of clustered sources [45, 68, 34].

We structure the rest of the paper as follows. Section 2 is a general description of QFS for evaluation in exterior domains, and proves (along with Appendix A) robustness criteria for Laplace, Helmholtz, and Stokes PDEs in 2D and 3D. The respective BVPs and fundamental solutions are also reviewed. Section 3 presents implementations in 2D of the two variants: QFS-B (Section 3.1) uses  $\partial\Omega$  as the check curve, while QFS-D (Section 3.4) uses a displaced check curve. The other subsections supply 2D convergence theory, and one-body numerical tests. Section 4 gives performance tests of FMM-accelerated QFS-D for large-scale 2D Helmholtz and Stokes BVPs (via geometry generation in Appendix B). Section 5 presents a preliminary 3D Laplace test involving ellipsoids. We draw conclusions in Section 6.

We host a Python implementation of QFS at <https://github.com/dbstein/qfs> MATLAB codes for some of 2D and 3D tests are also to be found at <https://github.com/ahbarnett/QFS>

### 1.1 Prior work on singular and near-singular BIE quadratures for smooth boundaries

Here we give a brief and incomplete review of the large literature on high-order Nyström quadratures in 2D and 3D. For background we suggest [59, 19, 5, 18, 70, 39]. (We do not address Galerkin discretizations, which have similar challenges.)

We first highlight some methods for task 1: filling  $A$ . The density  $\tau$  on  $\partial\Omega$  is represented by an *interpolant* from  $\tau$ , its samples at nodes. Nyström’s original method [59, Ch. 12.2] uses the kernel itself as interpolant, but this only applies to smooth kernels (double-layers for zero-frequency PDEs in 2D). Other cases need accurate integration of the product of each interpolatory basis function (which may be *global* or *panel-based*) with the weakly-singular kernel. For 2D Helmholtz, Kress [58] proposed a global product quadrature, which needs analytic insight to split off the logarithmically-singular part; an analogous 3D product quadrature uses spherical harmonics [28, 90]. Other 2D and 3D approaches include local weight corrections of the existing grid [51, 97, 98], and interpolating to custom *auxiliary quadrature nodes* [3, 64], where in 3D a local polar transformation can remove the singularity [14, 101, 13, 32].

We turn to task 2: evaluation near the boundary  $\partial\Omega$ . Here, in 2D and 3D, upsampling of a plain global rule gets accuracy nearer to  $\partial\Omega$  [5, 101], but cannot approach  $\partial\Omega$  [6]. Per-target *local* upsampling can be very efficient in 3D [36]. In 2D, Cauchy’s theorem is a powerful tool, either globally via barycentric evaluation [44, 9], or via panel monomial bases [44, 43, 99]. The idea of extrapolation towards  $\partial\Omega$  from near-surface data evaluated by an upsampled plain rule underpins quadrature by expansion [56, 6, 95, 81, 2] and “hedgehog” [72] schemes, as it does our proposal. Other approaches include density interpolation via Green’s theorem [76], regularization [10], and asymptotics [15]. Yet, for the exterior of the sphere, *uniform analytic expansions* of the potential are available [21, 100]; the wish to extend this to general shapes inspired this work.

Finally, we note the interplay between the two tasks: on-surface evaluation can aid with task 2, while many of the above off-surface methods can be, and are in practice, applied to task 1. The latter will also be true for our proposal.

## 2 Description of QFS and theoretical background for three PDEs

We present two variants of “quadrature by fundamental solutions”, each of which can evaluate layer potentials at targets far from, near to, or on,  $\partial\Omega$ :

1. QFS-B: The boundary  $\partial\Omega$  itself is used as the check surface, which requires the user to supply a Nyström (on-surface self-interaction) matrix  $A$ . (In the name, “B” stands for boundary.)
2. QFS-D: A new check surface is used on the opposite side of  $\partial\Omega$  from the proxy sources, thus the scheme is fully “desingularized” (hence “D”). Only a smooth *upsampling* scheme on  $\partial\Omega$  is needed. In addition it provides a method to fill  $A$  (task 1) without singular on-surface quadratures.

Both schemes have utility in applications; if the  $A$  matrix is already available then QFS-B is more convenient.

Given a density  $\tau$  on a boundary  $\partial\Omega$ , and desired layer potential representation (3) for  $u$  in the exterior of  $\Omega$ , both variants of QFS use new layer potentials placed on  $\gamma \in \Omega$ , an auxiliary closed curve in  $d = 2$  or surface in  $d = 3$ ,

$$\tilde{u}(\mathbf{x}) \approx [(\tilde{\alpha}\mathcal{S}_\gamma + \tilde{\beta}\mathcal{D}_\gamma)\sigma](\mathbf{x}), \quad \mathbf{x} \in \mathbb{R}^d \setminus \Omega. \quad (6)$$

Here  $\mathcal{S}_\gamma$  and  $\mathcal{D}_\gamma$  denote single- and double-layer potentials on  $\gamma$ , and the QFS mixing parameters  $(\tilde{\alpha}, \tilde{\beta})$  are generally distinct from  $(\alpha, \beta)$  in (3). To solve for the QFS source function  $\sigma$ , one collocates on a check curve (or surface)  $\gamma_c = \partial\Omega$  (for QFS-B), or  $\gamma_c$  exterior to and enclosing  $\overline{\Omega}$  (for QFS-D; see Fig. 1(d)). The desired Dirichlet data to match, which we call  $u_c$ , is given simply by evaluating the user-supplied potential,

$$u_c := [(\alpha\mathcal{S} + \beta\mathcal{D})\tau]|_{\gamma_c}. \quad (7)$$

For now we specialize to QFS-B where  $\gamma_c = \partial\Omega$ , so that care must be taken to use the exterior limit (jump relation), giving

$$u_c = [\alpha\mathcal{S} + \beta(\tfrac{1}{2}I + D)]\tau \quad (\text{matching data, continuous QFS-B case}). \quad (8)$$

Equating (6) to  $u_c$  on  $\gamma_c$  then gives the *first-kind integral equation* for  $\sigma$ ,

$$\int_{\gamma} \left( \tilde{\alpha}G(\mathbf{x}, \mathbf{y}) + \tilde{\beta} \frac{\partial G(\mathbf{x}, \mathbf{y})}{\partial \mathbf{n}_{\mathbf{y}}} \right) \sigma(\mathbf{y}) d\mathbf{s}_{\mathbf{y}} = u_c(\mathbf{x}), \quad \mathbf{x} \in \gamma_c \quad (9)$$

where for simplicity for now we use notation for the DLP valid only for scalar PDEs.

We discretize (9) by applying quadrature on  $\gamma$  with source nodes  $\{\mathbf{y}_j\}_{j=1}^P$ , and discrete collocation on  $\gamma_c = \partial\Omega$  at the user-supplied nodes  $\{\mathbf{x}_i\}_{i=1}^N$ , to get the  $N \times P$  linear system

$$\sum_{j=1}^P \left[ \tilde{\alpha} G(\mathbf{x}_i, \mathbf{y}_j) + \tilde{\beta} \frac{\partial G(\mathbf{x}_i, \mathbf{y}_j)}{\partial \mathbf{n}_{\mathbf{y}_j}} \right] \sigma_j = u_c(\mathbf{x}_i), \quad i = 1, \dots, N. \quad (10)$$

The right-hand side vector is given by  $\mathbf{u}_c := \{u_c(\mathbf{x}_i)\}_{i=1}^N \approx A\boldsymbol{\tau}$ , where  $A$  is the user-supplied exterior-limit Nyström matrix, and  $\boldsymbol{\tau} := \{\tau(\mathbf{x}_i)\}_{i=1}^N$  the user-supplied density vector. Note that quadrature weights on  $\gamma$  could be included; here for simplicity we left them implicit in  $\sigma_j$ . The linear system (10) needs a direct solution, due to its poor conditioning, to get  $\boldsymbol{\sigma} := \{\sigma_j\}_{j=1}^P$ . Finally, the discretization of (6),

$$\tilde{u}(\mathbf{x}) := \sum_{j=1}^P \left[ \tilde{\alpha} G(\mathbf{x}, \mathbf{y}_j) + \tilde{\beta} \frac{\partial G(\mathbf{x}, \mathbf{y}_j)}{\partial \mathbf{n}_{\mathbf{y}_j}} \right] \sigma_j, \quad \mathbf{x} \in \mathbb{R}^d \setminus \Omega, \quad (11)$$

defines our approximate QFS evaluation method for  $u$  at all target points  $\mathbf{x}$ . This completes the simplest mathematical description.

## 2.1 Analysis of continuous QFS for the exterior Laplace case

While appealing, the above proposal raises questions: What source curve/surface  $\gamma$  and mixing parameters  $(\tilde{\alpha}, \tilde{\beta})$  should be chosen? Is the choice to match Dirichlet data on  $\gamma_c$  robust? We first give theoretical results in the continuous case for the Laplace PDE, exterior case, covering both  $d = 2$  (which has a curious twist) and  $d = 3$ , then distill into criteria for more general elliptic PDE.

Recall that the exterior Laplace Dirichlet BVP is, given  $f \in C(\partial\Omega)$  and, in  $d = 2$  also a *total charge*  $\Sigma \in \mathbb{R}$ , to solve for  $u$  obeying

$$\Delta u = 0 \quad \text{in } \mathbb{R}^d \setminus \overline{\Omega} \quad (12)$$

$$u = f \quad \text{on } \partial\Omega \quad (13)$$

$$u(\mathbf{x}) = \begin{cases} \Sigma \log r + \omega + o(1), & d = 2, \\ o(1), & d = 3, \end{cases} \quad r := \|\mathbf{x}\| \rightarrow \infty, \text{ uniformly in angle.} \quad (14)$$

This has a unique solution ([59, Thm. 6.24] when  $\Sigma = 0$ , otherwise see [46, Sec. 1.4.1]). In  $d = 2$  the *constant term*  $\omega \in \mathbb{R}$ , which we emphasize is not part of the input data, may be extracted after solution as  $\omega = \lim_{\|\mathbf{x}\| \rightarrow \infty} u(\mathbf{x}) - \Sigma \log \|\mathbf{x}\|$ .

The subtlety in  $d = 2$  is that the desired Laplace layer potentials (3) on  $\partial\Omega$ , while exterior Laplace solutions, do *not* span the subspace of exterior harmonic functions obeying (14): in particular they are restricted to the subspace with  $\omega = 0$ . To see this, recall the Laplace fundamental solution

$$G(\mathbf{x}, \mathbf{y}) = \begin{cases} \frac{1}{2\pi} \log \frac{1}{r}, & d = 2, \\ \frac{1}{4\pi r}, & d = 3, \end{cases} \quad r := \|\mathbf{x} - \mathbf{y}\|. \quad (15)$$

Well known asymptotics [59, (6.14-15)] as  $r := \|\mathbf{x}\| \rightarrow \infty$  mean that any Laplace SLP with density  $\tau$  has the asymptotic  $C \log r + \mathcal{O}(1/r)$  in  $d = 2$ , where  $2\pi C = \int_{\partial\Omega} \tau$  is

the total charge. In  $d = 3$  the SLP is  $\mathcal{O}(1/r)$ . The DLP has the bound  $\mathcal{O}(1/r^{d-1})$  in  $d = 2, 3$ . Thus a mixture (3) has asymptotic  $\alpha C \log r + o(1)$  in  $d = 2$ , or  $o(1)$  in  $d = 3$ . A similar asymptotic of course holds for the QFS representation (6).

Does matching Dirichlet data  $u_c$  on  $\gamma_c = \partial\Omega$  proposed in (7)–(9) lead to a QFS approximation  $\tilde{u}$  equaling the correct exterior potential  $u$ ? In  $d = 3$  the answer must be yes, assuming (6) spans all possible  $u_c$ , by uniqueness of the exterior Dirichlet BVP. To handle the  $d = 2$  case we need to flip the roles of  $\Sigma$  and  $\omega$  to consider a modified BVP where the constant term is given (zero), but not the total charge (logarithmic growth). The following lemma shows that this is almost always possible.

**Lemma 2 (Modified exterior BVP in  $d = 2$ )** *Let  $\Omega \subset \mathbb{R}^2$  be a bounded domain with logarithmic capacity  $C_\Omega \neq 1$ . Then the “zero constant term exterior Dirichlet Laplace BVP,” where Dirichlet data  $f$  on  $\partial\Omega$  is specified plus the decay condition  $C \log r + o(1)$  as  $r \rightarrow \infty$  with  $C \in \mathbb{R}$  unknown, has a unique solution.*

*Proof* Let  $v$  solve the standard BVP (12)–(14) with data  $f$  and  $\Sigma = 0$ . Let  $\omega = v_\infty := \lim_{\|\mathbf{x}\| \rightarrow \infty} w(\mathbf{x})$  be its constant term. Let  $w$  solve the BVP (12)–(14) with  $f \equiv 0$  and  $\Sigma = 1$ ; so  $w$  is the Green function for  $\Omega$  with a pole at infinity, and by definition  $\log C_\Omega = -w_\infty := -\lim_{\|\mathbf{x}\| \rightarrow \infty} w(\mathbf{x}) + \log \|\mathbf{x}\|$  [65, Sec. 4.2]. Note that  $w_\infty$  is called the *Robin constant* for  $\Omega$ . If  $C_\Omega \neq 1$ , then  $v - \omega w / (\log C_\Omega)$  solves the modified BVP stated in the Lemma, with resulting logarithmic constant

$$C = -\omega / (\log C_\Omega) . \quad (16)$$

Failure when  $C_\Omega = 1$  can occur, as illustrated by  $\partial\Omega$  the unit circle, for which  $f \equiv 0$  gives a 1-dimensional subspace  $c \log r$ ,  $c \in \mathbb{R}$ , of solutions to the modified BVP in the lemma. For  $f \equiv 1$ , this BVP has no solution.

Armed with the above uniqueness results, we state our main result for Laplace (proved in Appendix A). It shows that: i) apart from unit logarithmic capacity in  $d = 2$ , QFS-B as presented above is robust for analytic data and surfaces, when the surface  $\gamma$  is chosen appropriately; ii) for this a pure SLP  $(\tilde{\alpha}, \tilde{\beta}) = (1, 0)$  is sufficient as the QFS mixture. The latter has an advantage over the obvious choice  $(\tilde{\alpha}, \tilde{\beta}) = (\alpha, \beta)$ , both in simplicity and numerical speed.

**Theorem 3 (QFS robustness for exterior Laplace)** *Let  $u$  be a Laplace solution in  $\mathbb{R}^d \setminus \overline{\Omega}$  with  $u = u_c$  on  $\partial\Omega$ , and decay conditions  $u(\mathbf{x}) = C \log r + o(1)$  for some  $C$  if  $d = 2$  (ie, zero constant term), or  $u(\mathbf{x}) = o(1)$  if  $d = 3$ , for  $r := \|\mathbf{x}\| \rightarrow \infty$ . Let  $u$  also continue analytically as a regular Laplace solution throughout the closed annulus (or shell) between  $\partial\Omega$  and a simple smooth interior surface  $\gamma \subset \Omega$ . Then the first kind integral equation*

$$\int_{\gamma} G(\mathbf{x}, \mathbf{y}) \sigma(\mathbf{y}) d\mathbf{s}_{\mathbf{y}} = u_c(\mathbf{x}), \quad \mathbf{x} \in \partial\Omega \quad (17)$$

*has a solution  $\sigma \in C^\infty(\gamma)$ . If  $d > 2$ , or the logarithmic capacity  $C_\Omega \neq 1$ , the solution is unique, and*

$$u(\mathbf{x}) = \int_{\gamma} G(\mathbf{x}, \mathbf{y}) \sigma(\mathbf{y}) d\mathbf{s}_{\mathbf{y}} , \quad \mathbf{x} \in \mathbb{R}^d \setminus \Omega . \quad (18)$$

Since layer potentials (3) obey the stated decay conditions, this shows that, at least for densities sufficiently analytic to allow  $u$  to continue as an interior PDE solution up to the source curve  $\gamma$ , QFS is robust. In  $d = 2$ , where complex analysis is available, it is known (eg [6, Prop. 3.1]) that  $u$  continues as a regular PDE solution as least as far into the nonphysical domain as the density  $\tau$  continues analytically from  $\partial\Omega$ . In  $d = 3$  results on analytic continuation are uncommon [50].

We will show shortly in Remark 12 how numerically to overcome the failure of Dirichlet matching for the troublesome case  $C_\Omega = 1$  in  $d = 2$ .

## 2.2 Background and robustness results for exterior evaluation for other PDEs

From the above Laplace analysis we can distill two criteria that together guarantee that QFS is a robust and accurate exterior layer potential evaluator for elliptic PDEs:

- C1) (Completeness.) In the evaluation region  $\mathbb{R}^d \setminus \overline{\Omega}$ , the range of  $\tilde{u}$  generated by densities  $\sigma$  in the QFS representation (6) contains the range of  $u$  generated by densities  $\tau$  in (3).
- C2) (Uniqueness.) There exists a linear subspace of exterior PDE solutions in  $\mathbb{R}^d \setminus \overline{\Omega}$  that contains the range of QFS representations (6), and in which imposing the matching data type on  $\gamma_c$  leads to *uniqueness within this subspace*.

It is easy to check that C1 plus C2 implies robustness for QFS.

To illustrate, in the above Laplace case, C1 (the fact that the pure SLP QFS representation spans the potentials generated by (3)) is assured, at least for sufficiently analytic  $\tau$ , by Theorem 3. Both of these representations lie in the subspace of exterior harmonic functions with decay as in the hypothesis of Theorem 3 (ie, zero constant term), which serves as the subspace in C2. Apart from when  $C_\Omega = 1$  in  $d = 2$ , C2 holds, since *within that subspace* Dirichlet data leads to uniqueness (Lemma 2). The subtlety of the failure for  $C_\Omega = 1$  is that, while (9) is still soluble (shown by construction in the proof of Theorem 3), its lack of uniqueness will lead numerically to  $\tilde{u}$  values different from  $u$  outside  $\partial\Omega$ .

**Remark 4** *These issues appear specific to exterior BVPs. Hence we need not (and do not) discuss the simpler interior case much in this work. We routinely use QFS for interior problems without issue, for example the enclosing boundary in Section 4.3.*

We now apply these criteria to show robustness for QFS in the examples of Helmholtz and Stokes layer potential evaluation. We will first need standard background material for these PDEs. The full theorems are deferred to the Appendix.

**Helmholtz.** The exterior Dirichlet BVP is, given any wavenumber  $k > 0$  and complex function  $f \in C(\partial\Omega)$ , to solve

$$(\Delta + k^2)u = 0 \quad \text{in } \mathbb{R}^d \setminus \overline{\Omega} \quad (19)$$

$$u = f \quad \text{on } \partial\Omega \quad (20)$$

$$\partial u / \partial r - iku = o(r^{-(d-1)/2}), \quad r := \|\mathbf{x}\| \rightarrow \infty, \quad (21)$$

where the last is the Sommerfeld radiation condition. This has a unique solution (see [19, p. 67] for  $d = 2$  and [19, Thm. 3.7] for  $d = 3$ ). The fundamental solution at wavenumber  $k > 0$  is [19, Sec. 2.2, 3.4]

$$G(\mathbf{x}, \mathbf{y}) = \begin{cases} \frac{i}{4} H_0^{(1)}(kr), & d = 2, \\ \frac{e^{ikr}}{4\pi r}, & d = 3, \end{cases} \quad r := \|\mathbf{x} - \mathbf{y}\|, \quad (22)$$

where  $H_0^{(1)}$  is the outgoing Hankel function of order zero. The resulting SLP and DLP also generate Helmholtz solutions obeying (21) [19, Sec. 3.1], so that C2 holds for this subspace. Theorem 26 then shows that C1 is satisfied when using the “combined field” mixture  $(\tilde{\alpha}, \tilde{\beta}) = (-i\eta, 1)$ , for  $\eta$  any nonzero real number. Following standard practice we choose  $\eta = k$  from now on [57]. The proof illustrates that a pure SLP or DLP would lead to nonrobustness for  $k^2$  a Neumann or Dirichlet (respectively) eigenvalue of the Laplacian in the interior of  $\gamma$ .

**Stokes.** We refer the reader to Ladyzhenskaya [62] and Hsiao-Wendland [46, Sec. 2.3] for background. The exterior Dirichlet BVP is, given constant fluid viscosity  $\mu > 0$ , velocity data  $\mathbf{f} \in C(\partial\Omega)^d$ , and in  $d = 2$  a growth condition  $\boldsymbol{\Sigma} \in \mathbb{R}^2$ , to solve for a velocity vector field  $\mathbf{u}$  and pressure scalar field  $p$  obeying

$$-\mu\Delta\mathbf{u} + \nabla p = 0 \quad \text{in } \mathbb{R}^d \setminus \overline{\Omega} \quad (23)$$

$$\nabla \cdot \mathbf{u} = 0 \quad \text{in } \mathbb{R}^d \setminus \overline{\Omega} \quad (24)$$

$$\mathbf{u} = \mathbf{f} \quad \text{on } \partial\Omega \quad (25)$$

$$\mathbf{u}(\mathbf{x}) = \begin{cases} \boldsymbol{\Sigma} \log r + \boldsymbol{\omega} + o(1), & d = 2, \\ o(1), & d = 3, \end{cases} \quad r := \|\mathbf{x}\| \rightarrow \infty. \quad (26)$$

This has a unique solution for  $\mathbf{u}$ , and  $p$  is unique up to an additive constant [62, p. 60] [46, Sec. 2.3.2]. In  $d = 2$  the constant term may be extracted from the solution via  $\boldsymbol{\omega} = \lim_{r \rightarrow \infty} \mathbf{u}(\mathbf{x}) - \boldsymbol{\Sigma} \log \|\mathbf{x}\|$ , thus when  $\mathbf{f} \equiv \mathbf{0}$  the BVP defines a  $2 \times 2$  matrix mapping  $\boldsymbol{\Sigma}$  to  $\boldsymbol{\omega}$ . The (tensor-valued) fundamental solution for velocity is

$$G(\mathbf{x}, \mathbf{y}) = \begin{cases} \frac{1}{4\pi\mu} \left( I \log \frac{1}{r} + \frac{\mathbf{r}\mathbf{r}^T}{r^2} \right), & d = 2, \\ \frac{1}{8\pi\mu} \left( I \frac{1}{r} + \frac{\mathbf{r}\mathbf{r}^T}{r^3} \right), & d = 3, \end{cases} \quad \mathbf{r} := \mathbf{x} - \mathbf{y}, \quad r := \|\mathbf{r}\|. \quad (27)$$

In contrast to the above scalar PDEs, the DLP kernel is not  $\partial G(\mathbf{x}, \mathbf{y}) / \partial \mathbf{n}_{\mathbf{y}}$ . The Stokes DLP kernel is

$$D(\mathbf{x}, \mathbf{y}) = \begin{cases} \frac{1}{\pi} \frac{(\mathbf{r} \cdot \mathbf{n}_{\mathbf{y}}) \mathbf{r} \mathbf{r}^T}{r^4}, & d = 2, \\ \frac{3}{4\pi} \frac{(\mathbf{r} \cdot \mathbf{n}_{\mathbf{y}}) \mathbf{r} \mathbf{r}^T}{r^5}, & d = 3. \end{cases} \quad (28)$$

Also, in  $d = 2$  the corresponding pressure kernels (65) will later be needed.

The goal is to evaluate velocities due to arbitrary densities  $\boldsymbol{\tau}$  in  $\mathbf{u} = (\alpha\mathcal{S} + \beta\mathcal{D})\boldsymbol{\tau}$ , the vector version of (3). Theorem 27 shows that the “completed” mixture  $(\tilde{\alpha}, \tilde{\beta}) = (1, 1)$  is robust, for all sufficiently analytic  $\boldsymbol{\tau}$ , in  $d = 3$ , or when the above  $2 \times 2$  matrix is nonsingular. The latter condition is analogous to the Laplace capacity condition; see Remark 13. (We also see numerically, and can prove, that a pure SLP  $(\tilde{\alpha}, \tilde{\beta}) = (1, 0)$  is robust for any  $\boldsymbol{\tau}$  which creates zero *net fluid flux*  $\beta \int_{\partial\Omega} \boldsymbol{\tau} \cdot \mathbf{n} = 0$ , as occurs in rigid-body flows.) The SLP and DLP generate Stokes solutions  $(\mathbf{u}, p)$  obeying (26), with  $\boldsymbol{\omega} = \mathbf{0}$  in  $d = 2$ , so that C2 holds for this zero-constant-term subspace. Finally, the theorem then shows that C1 is satisfied. We note that in  $d = 3$  a related MFS-based Stokes BIE method has been analysed [33].

### 3 The method for smooth curves in two dimensions

Here we first describe QFS-B for the exterior of a single boundary curve in 2D. We next give some theoretical justifications for the source location algorithm. We then show numerical tests of QFS-B, and finally describe and test QFS-D.

---

**Algorithm 1** Choosing source locations in 2D

---

**Require:**  $C^2$ -smooth parameterization  $\mathbf{x}(t)$  of  $\partial\Omega$ , user number of nodes  $N$ , user tolerance  $\epsilon$ , source upsampling parameter  $v \geq 1$  (by default 1).

- 1: assign  $P \leftarrow N$
- 2: assign a separation  $\delta$  appropriate for the user tolerance  $\epsilon$ , via

$$\delta = \frac{1}{P} \log \frac{1}{\epsilon} . \quad (31)$$

- 3: **if** the curve  $\gamma_\delta$  defined by (30) self-intersects or falls outside of  $\Omega$  **then**
- 4:   estimate  $\delta_0$  as the supremum of  $\delta$  values such that  $\gamma_\delta$  does not self-intersect nor fall outside of  $\Omega$
- 5:   reassign  $\delta \leftarrow \delta_0$   $\triangleright$  this brings source curve closer to  $\partial\Omega$
- 6:   reassign  $P$  via (31)  $\triangleright$  this increases  $P$
- 7: reassign  $P \leftarrow \lceil vP \rceil$   $\triangleright$  possibly upsample, round up
- 8: return  $P$  source locations  $\mathbf{y}_j$  on  $\gamma_\delta$  via

$$\mathbf{y}_j = \mathbf{x}(t_j) - \delta \|\mathbf{x}'(t_j)\| \mathbf{n}(t_j) + \delta^2 \mathbf{x}''(t_j) , \quad t_j = 2\pi j/P , \quad j = 1, \dots, P . \quad (32)$$


---

### 3.1 Basic 2D scheme using collocation on the boundary (QFS-B)

The user of QFS defines the boundary  $\partial\Omega$  by supplying a set of nodes  $\mathbf{x}_j \in \partial\Omega$  and weights  $w_j$ ,  $j = 1, \dots, N$ , which are a good quadrature rule for boundary integrals, meaning that

$$\int_{\partial\Omega} f(\mathbf{x}) ds_{\mathbf{x}} \approx \sum_{j=1}^N f(\mathbf{x}_j) w_j \quad (29)$$

holds for all smooth functions  $f$  on  $\partial\Omega$ . Specifically we assume that the error (relative difference between left and right sides) is no larger than the user-requested tolerance  $\epsilon$  for all “relevant” functions  $f$ , such as BIE integrands with distant targets. The user also supplies their vector of density values  $\tau_j := \tau(\mathbf{x}_j)$  at these nodes. The goal is then to evaluate a potential of the form (3) everywhere in the exterior, also with error  $\mathcal{O}(\epsilon)$ .

We now set up  $P$  sources at locations  $\mathbf{y}_j$ ,  $j = 1, \dots, P$ . For efficiency reasons we prefer that  $P = N$ , although it will sometimes need to be slightly larger. We assume that a smooth  $2\pi$ -periodic counterclockwise parameterization of  $\mathbf{x} : \mathbb{R} \rightarrow \mathbb{R}^2$  of  $\partial\Omega$  is available, meaning that  $\mathbf{x}([0, 2\pi)) = \partial\Omega$ , and  $\mathbf{x}(2\pi) = \mathbf{x}(0)$ . Such a parameterization (and its derivatives) can in practice be extracted by spectral interpolation from user-supplied nodes. Our recipe for source locations is then equispaced in parameter on an interior curve  $\gamma$  controlled by a separation parameter  $\delta > 0$ ,

$$\gamma_\delta := \{ \mathbf{x}(t) - \delta \|\mathbf{x}'(t)\| \mathbf{n}(t) + \delta^2 \mathbf{x}''(t) : 0 \leq t < 2\pi \} , \quad (30)$$

where  $\mathbf{n}(t) := R_{-\pi/2} \mathbf{x}'(t) / \|\mathbf{x}'(t)\|$  is the parametrized outward unit normal,  $R_\theta$  denoting counterclockwise rotation by  $\theta$ . We now propose to set  $\delta$  and  $P$ , and choose source locations  $\mathbf{y}_j \in \gamma_\delta$  equispaced in parameter, via Algorithm 1. To first order, this separates sources from  $\partial\Omega$  by a constant multiple of the local node spacing  $h$  on  $\partial\Omega$ ; for an example see Fig. 1(c).

As described early in Section 2, one now fills the dense “boundary from source” matrix  $B$  with entries as in (10),

$$B_{ij} = \tilde{\alpha} G(\mathbf{x}_i, \mathbf{y}_j) + \tilde{\beta} \frac{\partial G(\mathbf{x}_i, \mathbf{y}_j)}{\partial \mathbf{n}_{\mathbf{y}_j}} , \quad i = 1, \dots, N, \quad j = 1, \dots, P , \quad (33)$$



where we state only the scalar case (in the vector case each entry is a  $2 \times 2$  matrix). The action of  $B$  is sketched in Fig. 1(c). Recall that, given the user-supplied density vector  $\boldsymbol{\tau}$ , Dirichlet matching data is evaluated via

$$\mathbf{u}_c = A\boldsymbol{\tau} , \quad (34)$$

where  $A$  is a user-supplied exterior limit Nyström matrix (as in (4)–(5)).

Mathematically, one then solves for the vector  $\boldsymbol{\sigma} \in \mathbb{C}^P$  in the linear system

$$B\boldsymbol{\sigma} = \mathbf{u}_c , \quad (35)$$

which abbreviates (10), and is interpreted as matching  $\tilde{u}$  in (11) to  $u_c$  on  $\partial\Omega$ , then applies (11) as the QFS approximation to  $u$  for all exterior target points.

Since it is inefficient to do the dense solve of (34)–(35) anew for each density, we propose the following variant, firstly in exact arithmetic. One precomputes the  $P \times N$  matrix solution  $X$  to the matrix equation

$$BX = A . \quad (36)$$

The action of  $X$  is sketched in Fig. 1(c). Then, for each new  $\boldsymbol{\tau}$  vector, one takes the product

$$\boldsymbol{\sigma} = X\boldsymbol{\tau} \quad (37)$$

to give the desired  $\boldsymbol{\sigma}$  in only  $\mathcal{O}(N^2)$  time per vector. It is easy to check that (36)–(37) solves (34)–(35) in exact arithmetic.

However (36)–(37) is unstable in finite-precision arithmetic because the entries of  $X$  are large, due to the ill-conditioning of  $B$  (which is exponentially bad, as we will quantify in Proposition 9). Catastrophic cancellation in applying (37) typically loses several digits of accuracy; this cannot be avoided if  $X$  is formed. Thus, instead, following [63, Rmk. 5] [69] we propose storing  $X$  as two factors  $X = YZ$ . Taking the SVD of  $B$  (which, since  $P \geq N$ , is either square or “tall”),

$$U\Sigma V^* = B , \quad (38)$$

where  $\Sigma = \text{diag} \{s_j\}_{j=1}^N$ , the singular values being denoted by  $s_j$ , one then fills

$$Y = V\Sigma^{-1}, \quad Z = U^*A , \quad (39)$$

where  $\Sigma^{-1} := \text{diag} \{s_j^{-1}\}_{j=1}^N$ . New user-supplied density vectors can then be converted to QFS source vectors in  $\mathcal{O}(N^2)$  time via

$$\boldsymbol{\sigma} = Y(Z\boldsymbol{\tau}) , \quad (40)$$

where the *order of multiplication* implied by parenthesis is crucial for numerical stability. This concludes the basic QFS-B description in 2D; we will now motivate some aspects via more analytic results.

**Remark 5** *In practice, in 2D, although  $B$  is ill-conditioned, it is not sufficiently so that a regularized inverse is needed in (39). This is because sources chosen using (31), combined with the upcoming Proposition 9, predicts a minimum eigenvalue, hence singular value, of  $\mathcal{O}(\sqrt{\epsilon})$ , safely above  $\epsilon_{\text{mach}}$ .*

### 3.2 Discrete theory for source point choice and convergence rate in 2D

So far our analytic results have been at the continuous (integral operator) level. We now introduce analytical background for the *discrete* problem, to justify Algorithm 1 and to understand the convergence *rate* of QFS.

For this analysis, and later numerical tests, we specialize to quadrature of an analytic curve  $\partial\Omega$  deriving from the periodic trapezoid rule (PTR) [93]. Recall that for general  $2\pi$ -periodic functions  $g(t)$  the latter is

$$\int_0^{2\pi} f(t)dt \approx \frac{2\pi}{N} \sum_{j=1}^N f(2\pi j/N) \quad (\text{PTR}) , \quad (41)$$

and this rule is high-order accurate for  $g$  smooth. Moreover we have exponential convergence for  $g$  analytic.

**Theorem 6 (Davis [23])** *Let  $f$  be  $2\pi$ -periodic and analytic, and continue analytically to a function bounded uniformly in the closed strip  $|\text{Im } t| \leq d$ . Then the error in the PTR quadrature (difference between left and right sides of (41)) is  $\mathcal{O}(e^{-dN})$  as  $N \rightarrow \infty$ .*

Given a  $2\pi$ -periodic smooth parameterization  $\mathbf{x}(t)$  of  $\partial\Omega$ , a boundary quadrature rule (29) follows by changing variable from arclength to  $t$  then applying the PTR,

$$\int_{\partial\Omega} f(\mathbf{x})ds_{\mathbf{x}} = \int_0^{2\pi} f(\mathbf{x}(t))\|\mathbf{x}'(t)\| dt \approx \frac{2\pi}{N} \sum_{j=1}^N f(\mathbf{x}(2\pi j/N)) \|\mathbf{x}'(2\pi j/N)\|$$

implying that the nodes and weights in (29) are

$$\mathbf{x}_j = \mathbf{x}(2\pi j/N) , \quad w_j = (2\pi/N)\|\mathbf{x}'(2\pi j/N)\| . \quad (42)$$

Here  $\mathbf{x}'(t) := d\mathbf{x}/dt$  is the parametric “velocity”,  $\|\mathbf{x}'(t)\|$  its “speed”, so the local node spacing ( $h$ ) is  $w_j$ .

The source curve (30) proposed above has its origin as a 2nd-order Taylor approximation to the following curve  $\gamma_{\delta}^{\text{imag}}$  generated by “imaginary parameter translation”. Assume that the  $\partial\Omega$  parameterization  $\mathbf{x}(t) = [x_1(t), x_2(t)]$  is a pair of real analytic functions, and  $\|\mathbf{x}(t)\| > 0$ ,  $t \in [0, 2\pi)$ . In that case it is possible to analytically extend the parameterization into an annulus around  $\partial\Omega$  by identifying  $\mathbb{R}^2$  with  $\mathbb{C}$ , as follows. Let  $Z(t) := x_1(t) + ix_2(t)$  for  $t$  real, then  $Z$  may be uniquely analytically continued throughout some strip  $I_0 := \{t \in \mathbb{C} : |\text{Im } t| < \delta_0\}$  about the real axis, defining an annular conformal map  $Z : I_0 \rightarrow \mathbb{C}$ . Then define

$$\mathbf{x}(t, \delta) := [\text{Re } Z(t + i\delta), \text{Im } Z(t + i\delta)], \quad t, \delta \in \mathbb{R} , \quad (43)$$

and note that  $\mathbf{x}(t, 0) = \mathbf{x}(t)$  for all  $t$ , which recovers  $\partial\Omega$ . We call (43) an *imaginary shift by  $\delta$  in the complexified parameterization*. Fixing  $\delta$ , it generates a curve

$$\gamma_{\delta}^{\text{imag}} := \{\mathbf{x}(t, \delta) : 0 \leq t < 2\pi\} \quad (44)$$

which for  $\delta > 0$  lies inside  $\partial\Omega$ , and for  $\delta < 0$  lies outside  $\partial\Omega$ . In practice we find that the 2nd-order approximation is good, ie,  $\gamma_{\delta}$  is very close to  $\gamma_{\delta}^{\text{imag}}$ , and  $\|\mathbf{y}_j - \mathbf{x}(2\pi j/P, \delta)\| \ll \delta$ , making the following theory relevant.

The imaginary translation idea has been studied in the setting of the MFS, where it brings both practical and theoretical advantages [55, 52, 7, 49, 67]. It has led to a class of convergence results for various BVPs which can be summarized, somewhat loosely, by the following.

**Theorem 7 (MFS convergence rate [53, 55, 7, 49])** *Let the matching curve  $\gamma_c = \partial\Omega$  be analytic, as above, with  $Z$  analytic in a strip with half-width  $\delta_0$ . Let the data  $u_c$  on  $\partial\Omega$  be analytic, with parametric form  $u_c(t)$  continuing to an analytic function throughout some strip  $|\operatorname{Im} t| \leq \delta_*$ . Let  $\delta > 0$  be sufficiently small, generating source locations  $\mathbf{y}_j = \mathbf{x}(2\pi j/P, \delta)$ ,  $j = 1, \dots, P$ , and source mixture  $(\tilde{\alpha}, \tilde{\beta}) = (1, 0)$ . Then there is an algebraic order  $a \geq 0$  such that the (MFS or QFS) solution method (10)–(11) in exact arithmetic has asymptotic error*

$$\|\tilde{u} - u_c\|_{\partial\Omega} = \begin{cases} \mathcal{O}(P^a e^{-\delta P}), & \delta < \delta_*/2 & (\text{discrete source aliasing; smooth data}) \\ \mathcal{O}(P^a e^{-\delta_* P/2}), & \delta \geq \delta_*/2 & (\text{Nyquist frequency limit; rough data}) \end{cases} \quad (45)$$

as  $P \rightarrow \infty$ , where  $\|\cdot\|_{\partial\Omega}$  is some boundary norm.

Such results state that the MFS has near-exponential convergence in the number of source points, with two regimes of rate interpreted as follows: if the sources are *close* to  $\partial\Omega$  then their discrete aliasing error prevents each Fourier mode of  $u_c(t)$  from being accurately represented; whereas, if the sources are *far* from  $\partial\Omega$  the roughness of  $u_c$  dominates the error because they cannot represent Fourier modes on  $\partial\Omega$  with index magnitude exceeding the Nyquist frequency  $P/2$ .

**Remark 8** *The above theorem was first proven for the interior Laplace BVP in the disk by Katsurada [53], and generalized to interior Helmholtz in the disk with  $L^2$ -minimization on  $\partial\Omega$  in [7, Thm. 3]. These results used Fourier series in  $t$ , and in almost all cases there is no algebraic prefactor ( $a = 0$ ). For general analytic boundaries with annular conformal maps, only the second case in (45) is known for interior Laplace [54, Thm. 3.2] [55, App. A], while for exterior Helmholtz problems, Kangro [49, Thm 4.1] has proven the first case in (45). These latter results use integral operator approximations in exponentially-weighted Sobolev spaces, and involve quite technical other conditions that we do not state. We know of no such results for Stokes BVPs, even on the disk. So the analysis of the MFS, even for 2D analytic domains, is still incomplete.*

Our criterion (31) for  $\delta$  and  $P$  is now understood as follows: one sets the boundary error norm to the user-requested tolerance  $\epsilon$ , drops the algebraic prefactor in the upper (aliasing or smooth data) case of (45), then uses this as an equality. If the resulting curve  $\gamma_\delta$  self-intersects or falls outside of  $\Omega$ , then  $\delta > \delta_0$  was too large and Theorem 7 does not apply. This provides an analytic foundation for Algorithm 1.

The above MFS convergence theorems rely on the smoothness of the layer operators between separated curves. For the special case of concentric circles this smoothness is simple to show via polar separation of variables, giving the following general result for scalar 2nd-order elliptic PDE.

**Proposition 9 (ill-conditioning of first-kind integral equation)** *Consider  $\partial\Omega$  the unit circle with complexified parameterization  $Z(t) = e^{it}$ , and let  $\delta \neq 0$  so that  $\gamma_\delta^{\text{imag}}$  is the concentric circle of radius  $e^{-\delta} \neq 1$ . Then the single- and double-layer integral operators from source  $\gamma_\delta^{\text{imag}}$  to target  $\partial\Omega$  have as eigenvectors the Fourier modes  $e^{int}$ ,  $n \in \mathbb{Z}$ , with corresponding eigenvalues decaying as  $\mathcal{O}(e^{-|\delta n|})$  asymptotically as  $|n| \rightarrow \infty$ , ignoring algebraic prefactors.*

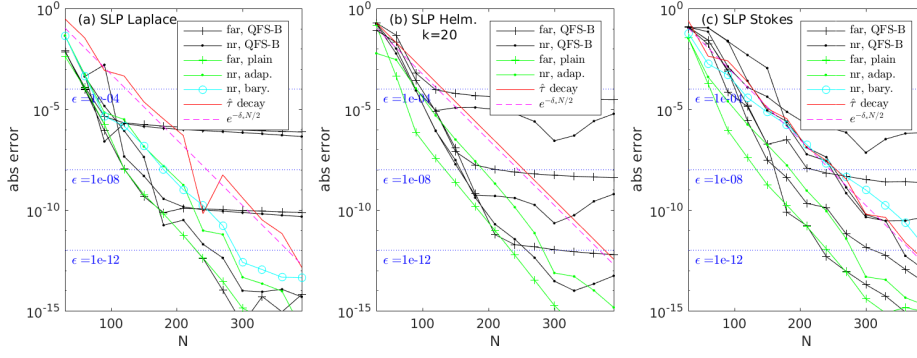


Fig. 2: Error convergence for 2D exterior evaluation of a given single-layer potential  $\tau$  vs number of nodes  $N$ , for 3 PDEs (a,b,c); see Sec. 3.3. The shape and (far, near) targets are as in Fig. 1. QFS-B from Sec. 3.1 is shown (black) for the three tolerances shown (blue). Green curves show the plain Nyström rule for the far target, and adaptive Gaussian integration of the spectral interpolant for the near target. The barycentric method of [9] is also shown for the near target (cyan circles). The Fourier decay (47) of the density (red) and a predicted rate based on  $\delta_*$  the parameter-plane singularity distance from the real axis (dashed) are compared.

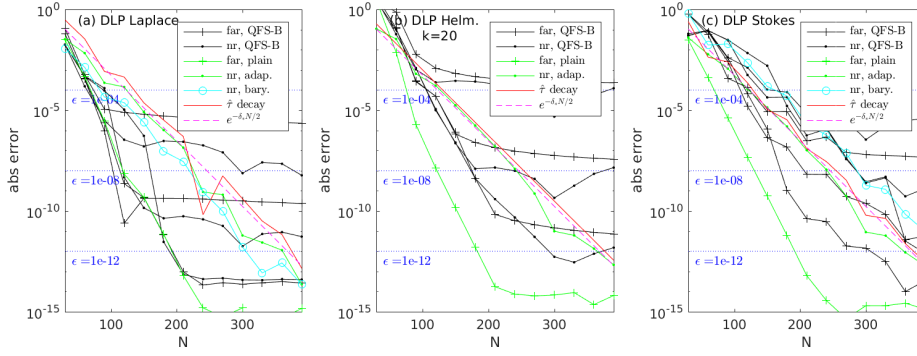


Fig. 3: Same as Fig. 2 but testing evaluation of the double-layer potential.

This is well known for Laplace and for fixed- $k$  Helmholtz (eg, see [7] for the single-layer case). For Stokes, numerically one sees similar upper (but not always lower) bounds; the analysis is incomplete (but see [47]). For general curves obtained by imaginary translations in the general annular conformal map case, similar results feature in the proofs of Theorem 7 in Laplace [55] and Helmholtz [49] settings.

**Remark 10 (upper bound on separation)** *Given finite-precision arithmetic, Proposition 9 implies that the source curve  $\gamma_\delta$  should not be so far from the check curve (in this case  $\partial\Omega$ ) that the influence on (eigenvalue of) the highest Fourier mode  $|n| = N/2$  on the boundary drops below machine precision,  $\epsilon_{\text{mach}}$ . This gives the upper bound on separation  $\delta \leq \frac{2}{N} \log \epsilon_{\text{mach}}^{-1}$ . We note that, since  $P \approx N$  and  $\epsilon > \epsilon_{\text{mach}}$ , the choice (31) is safely no more than about half this upper bound.*

### 3.3 Tests of QFS-B for Laplace, Helmholtz, and Stokes exterior evaluation

Here we test, for three PDEs, and three tolerances  $\epsilon$ , the error performance of QFS-B for evaluation of given single- or double-layer potentials (ie,  $(\alpha, \beta) = (1, 0)$  for SLP, or  $(0, 1)$  for DLP, in (3)). We use the same analytic starfish domain as in Fig. 1, for which the maximum non-intersecting  $\gamma$  separation distance is found numerically to be  $\delta_0 \approx 0.168$ . In each case we test far and near targets, measuring errors relative to fully-converged plain or adaptive integration, respectively. We work in MATLAB R2017 on a i7 CPU; calculations take only a few seconds. We are forced to test a quite large near-boundary distance of  $10^{-4}$  to retain all digits in adaptive integration (via MATLAB's `integral` command), due to catastrophic cancellation in the integrand. QFS, by contrast, can handle distances down to zero reliably.

**Laplace.** In QFS we use the pure SLP  $(\tilde{\alpha}, \tilde{\beta}) = (1, 0)$ , which is robust by Theorem 3. Recall the fundamental solution (15). For each  $N$  we use Algorithm 1, with  $v = 1$  so that  $P = N$  unless self-intersection triggered an increase in  $P$ . At  $\epsilon = 10^{-12}$ , in this domain, this was not triggered once  $N \geq 150$ . Fig. 2(a) compares the convergence of QFS-B to other standard methods, in a generic test case for evaluating a pure SLP, and Fig. 3(a) shows the same for evaluating a pure DLP. In both cases QFS-B shows very similar convergence to the gold-standard plain Nyström rule for the far target, and adaptive integration of the trigonometric (spectral) interpolant for a near target, down to the chosen tolerance  $\epsilon$ . When errors hit  $\epsilon$  (actually 1-2 digits below), they flatten out, as predicted by our separation choice (31). This, along with stability for larger  $N$ , indicates success. A barycentric Cauchy method (see [9] for SLP, [48, 44] for DLP) is also compared for the near target, and exhibits the same rate.

We now discuss some details about the density and convergence rates. For the test we chose a real-analytic density, in terms of the boundary parameter  $t$ ,

$$\tau(t) = [0.5 + \sin(3t + 1)] \operatorname{Re} \cot \frac{t - t_*}{2}, \quad t \in [0, 2\pi), \quad (46)$$

whose important feature is its complex singularity location  $t_* = 0.5 + i\delta_*$ , where  $\delta_* = 0.15$  controls its distance and hence smoothness along the real axis. Note that  $\delta_*$  is similar to the boundary's  $\delta_0$ ; this models low-frequency scattering problems, where data smoothness is controlled by the geometry. We have verified that the QFS performance is similar to gold-standard methods down to  $\epsilon$  also for other  $\delta_*$  choices.

An estimate of the ability of  $N$  boundary samples to capture any density  $\tau$  is the relative decay of its Fourier series  $\tau(t) = \sum_{n \in \mathbb{Z}} \hat{\tau}_n e^{int}$  at the Nyquist frequency  $n = N/2$ , which we measure by

$$r_N[\tau] := \frac{|\hat{\tau}_{N/2}|}{|\hat{\tau}_0|}. \quad (47)$$

This metric is included (in red) on the plots, and compared against its asymptotic prediction  $e^{-\delta_* N/2}$  (magenta) set by the known singularity; the match is excellent.

**Remark 11 (Laplace error decay rates)** *For the SLP in Fig. 2(a) we see that the Nyquist decay rate (red and pink) explains well the convergence of all the near-target methods. The far target rate is slightly faster. For the DLP in Fig. 3(a), in contrast, the plain Nyström rule for the far target has about twice the Nyquist rate, and QFS-B achieves this faster rate for both near and far targets. The doubling of rate for the plain rule is believed to be due to the fact that for a distant target the kernel is as smooth*

as the geometry, so that the PTR rate  $e^{-\delta_* N}$  of Theorem 6 is relevant, being twice the Nyquist rate. However, this does not explain why the rate for the SLP is less than doubled. We do not have an explanation for the doubling of the QFS-B DLP near rate.

**Remark 12 (robustness when the matching curve  $\partial\Omega$  has logarithmic capacity near 1.)**

Lemma 2, in particular (16), showed that numerical instability will occur when  $C_\Omega \approx 1$ : the Dirichlet matching on  $\partial\Omega$  becomes unable to determine the total charge  $\Sigma$ , which is crucial to accurate evaluation of  $u$ . However, given a desired representation (3), the total charge is in fact known:  $\Sigma = \alpha \int_{\partial\Omega} \tau$ . Thus, stability is easily recovered by adding one row to each matrix  $A$  and  $B$  that enforces this condition in (34)–(35). Specifically, we append to  $A$  the row  $\{\alpha w_j\}_{j=1}^N$  (where  $w_j$  are the weights in (42)), and to  $B$  the row of all ones. We have verified that in the case of  $\Omega$  the unit disk, where  $C_\Omega = 1$ , this modification turns complete failure into successful error convergence similar to that shown above. We need not show the plots.

**Helmholtz.** Recall that the fundamental solution is (22), and that we use a combined-field QFS representation. We again set source upsampling  $v = 1$ . For a complex-valued density  $\tau$  we choose (46) except with the Re operator removed, and fix  $k = 20$  (around 8 wavelengths across the domain). Fig. 2(b) compares the convergence of QFS-B for evaluating the pure SLP to the gold standard (as with Laplace, plain Nyström for the far target, and adaptive integration of the spectral interpolant for the near target). We again see success, meaning that the rates are similar and, although the error at which QFS-B saturates is 1-2 digits worse than for the Laplace case, it remains consistent with the requested tolerance  $\epsilon$ . We do not compare to a barycentric method, since we know of no such published method for Helmholtz. Fig. 3(b) shows similar performance for evaluating a pure DLP, although, as in Remark 11, there is a factor of two separating the gold-standard far and near convergence rates; QFS-B falls somewhere between the two rates. One also sees saturation about 1 digit worse than  $\epsilon$ , indicating that the user should set  $\epsilon$  slightly below their desired tolerance.

**Stokes.** Recall that we use a completed QFS representation  $S + D$ , and that the kernels are (27)–(28). We set viscosity to a generic near-unit value  $\mu = 0.7$ , and choose the vector-valued density function

$$\tau(t) = \text{Re} \begin{bmatrix} e^{4i} (0.5 + \sin(3t + 1)) \cot \frac{t-t_*}{2} \\ e^{5i} (0.5 + \cos(2t - 1)) \cot \frac{t-t_*}{2} \end{bmatrix}, \quad t \in [0, 2\pi), \quad (48)$$

Apart from its singularity distance  $\delta_* = 0.15$ , (48) is designed to be generic; eg, it has net flux  $\int_{\partial\Omega} \tau \cdot \mathbf{n} \neq 0$ . To achieve numerical and spectral stability (see the upcoming Fig. 5), for this PDE we need to set source upsampling to  $v = 1.3$  Fig. 2(c) and Fig. 3(c) then compare QFS-B against the same gold-standard methods used for Laplace, including the barycentric Stokes methods introduced in [9]. With this choice, QFS-B again matches well the gold-standard error convergence for SLP, and is close for DLP, down to below  $\epsilon$ . Together with stability at all  $N$ , this indicates success.

**Remark 13 (Stokes breakdown for certain domains?)** Unlike for Laplace where unit-capacity domains are easy to construct, we have not observed “in the wild” the Stokes QFS failure potentially allowed by Theorem 27. We also have not found literature about the possibility of the  $2 \times 2$  matrix becoming singular. For complete robustness, we have tested adding two extra rows to enforce the known  $\Sigma$  (analogous to Remark 12): this is successful for QFS-D, but limits near-target accuracy in QFS-B to about  $10^{-9}$ , an issue that we leave for future study.

### 3.4 Desingularized scheme using off-surface check points (QFS-D)

We now show how only upsampled off-surface evaluations can be used to evaluate layer potentials in the solution domain and on the boundary, including the filling of the Nyström  $A$  matrix (task 2). This makes QFS truly kernel-independent (apart from the choice of QFS representation  $(\tilde{\alpha}, \tilde{\beta})$  which may vary by PDE).

$P$  source points with separation parameter  $\delta$  are chosen via Algorithm 1, as in QFS-B. Then recalling (31), one chooses a check curve separation parameter  $\delta_c > 0$  via

$$\delta_c = \frac{1}{P} \log \frac{1}{\epsilon_{\text{mach}}} - \delta = \left( \frac{\log \epsilon_{\text{mach}}}{\log \epsilon} - 1 \right) \delta, \quad (49)$$

and if the resulting curve  $\gamma_{-\delta_c}$  self-intersects or hits  $\Omega$ ,  $\delta_c$  is reduced to the supremum of values,  $\delta_{c,0}$ , for which this no longer holds. The number of check points is  $M = \lceil v_c N \rceil$ , with  $v_c$  a small PDE-dependent upsampling parameter (by default 1). The check points  $\mathbf{z}_m$  are then

$$\mathbf{z}_m = \mathbf{x}(t_m) + \delta_c \|\mathbf{x}'(t_m)\| \mathbf{n}(t_m) + \delta_c^2 \mathbf{x}''(t_m), \quad t_m = 2\pi m/M, \quad m = 1, \dots, M, \quad (50)$$

noting the sign change which approximates an imaginary translation by  $-\delta_c$ . Fig. 1(d) shows source and check points when  $\epsilon = 10^{-12}$ ; note that the check points are around three times closer to  $\partial\Omega$  than the source points.

**Remark 14 (check point distance  $\delta_c$ )** *The heuristic observation behind (49) is that when collocation is performed to match potential values on  $\gamma_c$  to  $\mathcal{O}(\epsilon_{\text{mach}})$ , there is an exponential deterioration of errors as one moves off this curve back towards  $\partial\Omega$ , as expected because numerical analytic continuation as a PDE solution is involved. Its rate is such that  $\mathcal{O}(1)$  error is reached by  $\gamma$ , the source curve. Thus in order to insure the user-requested tolerance  $\epsilon$  on  $\partial\Omega$ , the ratio condition*

$$\frac{\delta}{\delta + \delta_c} \geq \frac{\log \epsilon}{\log \epsilon_{\text{mach}}} \quad (51)$$

*must hold. For example, when  $\epsilon = 10^{-12}$  and  $\epsilon_{\text{mach}} \approx 10^{-16}$ , the right-hand side is  $3/4$ , leading to  $\delta_c \leq \delta/3$ . Treating the condition as an equality leads to (49).*

The  $M \times P$  “check from source” matrix, which for QFS-D we now denote by  $E$ , is then filled with elements

$$E_{mj} = \tilde{\alpha} G(\mathbf{z}_m, \mathbf{y}_j) + \tilde{\beta} \frac{\partial G(\mathbf{z}_m, \mathbf{y}_j)}{\partial \mathbf{n}_{\mathbf{y}_j}}, \quad m = 1, \dots, M, \quad j = 1, \dots, P, \quad (52)$$

where as before we state only the scalar case. The action of  $E$  is sketched in Fig. 1(d). Since the separation parameter between source and check curves is no more than  $N^{-1} \log \epsilon_{\text{mach}}^{-1}$ , barring small upsampling factors, Remark 5 also applies to this  $E$  matrix.

The final ingredient is to evaluate  $u$  accurately on  $\gamma_c$  to get  $u_c$ . The user-supplied  $N$  nodes are rarely adequate for this, but plain quadrature from an *upsampled* set of nodes can be very accurate. The following result, for the PTR case, enables our choice of boundary upsampling factor.



**Theorem 15** [6, Thm. 2.3, 2.9] *Let  $\partial\Omega$  be analytic, and  $Z$  be the analytic continuation of its complex parameterization, with  $Z$  analytic and bijective in some strip  $I_0 = \{t \in \mathbb{C} : |\operatorname{Im} t| < \delta_0\}$ . Let  $\tau(t)$ ,  $t \in [0, 2\pi)$ , be an analytic density that continues analytically in  $I_0$ . Recalling (43), let  $\mathbf{x} = \mathbf{x}(t, \delta)$ , for arbitrary  $t \in \mathbb{R}$  and imaginary shift  $\delta \neq 0$ , be a target point. Then the error in applying the PTR (42) to evaluation of the Laplace layer potential (3) at this target point is  $\mathcal{O}(e^{-|\delta|N})$ , as  $N \rightarrow \infty$ .*

Thus the exponential convergence rate with the number of boundary nodes is the complexified parametric distance of the target from the source curve. The mechanism is the same as the upper case in (45). Its proof uses a modification of Theorem 6 to handle integrands with a single singularity or branch cut in the strip (annulus). The same rate is conjectured (and numerically verified) for Helmholtz [6] and Stokes [96].

Applying Theorem 15 (ignoring prefactors), to reach full accuracy  $\epsilon_{\text{mach}}$  at the check point imaginary translation of  $\delta_c$ , one needs  $\tilde{N} = \lceil \rho N \rceil$  boundary nodes, where the boundary upsampling factor  $\rho$  is

$$\rho = \max \left[ \frac{1}{\delta_c N} \log \frac{1}{\epsilon_{\text{mach}}}, 1 \right]. \quad (53)$$

Here the max prevents downsampling, which would be wasteful. For example,  $\epsilon = 10^{-4}$  results in  $\rho \approx 1.3$ , while  $\epsilon = 10^{-12}$  results in  $\rho \approx 4.3$ . The vector of check potentials is then evaluated by the upsampled plain rule,

$$\mathbf{u}_c = C\boldsymbol{\tau}, \quad \text{where} \quad C := \tilde{C}L_{\tilde{N} \times N}, \quad (54)$$

where  $\tilde{C}$  is an “check from upsampled boundary” matrix with elements

$$C_{mj} = \tilde{\alpha}G(\mathbf{z}_m, \tilde{\mathbf{x}}_j) + \tilde{\beta} \frac{\partial G(\mathbf{z}_m, \tilde{\mathbf{x}}_j)}{\partial \mathbf{n}_{\tilde{\mathbf{x}}_j}}, \quad m = 1, \dots, M, \quad j = 1, \dots, \tilde{N}, \quad (55)$$

where  $\tilde{\mathbf{x}}_j = \mathbf{x}(2\pi j/\tilde{N})$ ,  $j = 1, \dots, \tilde{N}$ , are spectrally upsampled boundary nodes. The matrix  $L_{\tilde{N} \times N}$  in (54) is a standard spectral upsampling matrix with elements

$$(L_{\tilde{N} \times N})_{lj} = \frac{1}{N} \phi_N(2\pi[l/\tilde{N} - j/N]), \quad l = 1, \dots, \tilde{N}, \quad j = 1, \dots, N, \quad (56)$$

where  $\phi_N(s) := 1 + 2 \sum_{k=1}^{N/2-1} \cos ks + \cos(N/2)s$  is a slight variant of the Dirichlet kernel function, and we took the case that  $N$  and  $\tilde{N}$  are both even. The upsampled boundary nodes (blue dots) and action of the  $M \times N$  evaluation matrix  $C$  in (54) are sketched in Fig. 1(d).

The dense factorization (precomputation stage) for QFS-D is very similar to QFS-B. In the simplest version one takes the SVD

$$U\Sigma V^* = E \quad (57)$$

then fills

$$Y = V\Sigma^{-1}, \quad Z = U^*C, \quad (58)$$

so that new density vectors may be converted to source vectors as before by (40). Algorithm 2 summarizes these two steps. The resulting sources may then be used to evaluate the potential everywhere via (11).

Finally, an approximation  $\tilde{A}$  to the Nyström self-interaction matrix (including the exterior limit  $\frac{\alpha}{2}I$  term due to the jump relation) is  $\tilde{A} = BX$ , recalling (36), with

---

**Algorithm 2** QFS-D (desingularized) for single body, tasks 1 and 2

---

- 1: **procedure** QFSDPRECOMPUTE( $N$  nodes  $\mathbf{x}_j$  describing  $\partial\Omega$ , tolerance  $\epsilon$ , mixture  $(\alpha, \beta)$ ,  
source and check upsampling parameters  $v, v_c \geq 1$ ) ▷ set-up,  $\mathcal{O}(N^3)$  work
  - 2:   Use the PDE type to choose robust QFS mixture  $(\tilde{\alpha}, \tilde{\beta})$  as in Sections 2.1–2.2.
  - 3:   Choose  $P$  source points  $\mathbf{y}_j$  (if  $d = 2$  use Algorithm 1)
  - 4:   Choose  $M$  check points  $\mathbf{z}_m$  (if  $d = 2$  use (49)–(50))
  - 5:   Choose boundary upsampling factor  $\rho$  via (53)
  - 6:   Fill matrices: “check from source”  $E$  via (52)
  - 7:                   “check from boundary”  $C$  via upsampling and matrix product (54)–(56)
  - 8:                   “boundary from source”  $B$  via (33)
  - 9:   Take SVD of  $E$  then form  $Y$  and  $Z$  via (58) ▷ (or LU as in Remark 17)
  - 10:   Form Nyström self-interaction matrix  $\tilde{A}$  via (59)
  - 11:   **return**  $Y, Z, \tilde{A}$  ▷ (or **return**  $L, U, \bar{P}C, \tilde{A}$ ; Remark 17)
  - 12: **procedure** QFSDAPPLY( $Y, Z$ , vector  $\boldsymbol{\tau}$  of  $N$  density samples) ▷ compute sources,  $\mathcal{O}(N^2)$
  - 13:   **return**  $\boldsymbol{\sigma} = Y(Z\boldsymbol{\tau})$  ▷ the layer potential  $u(\mathbf{x})$  may now be evaluated via (11)
- 

$B$  defined (in the scalar case) by (33), and  $X = YZ$ . While forming  $X$  then  $BX$  is adequate for a few digits of accuracy, full accuracy requires reordering as

$$\tilde{A} = (BY)Z, \quad (59)$$

to avoid catastrophic cancellations as in Sec. 3.1. After a couple of remarks, we proceed to numerical tests of the method.

**Remark 16** *The reader may wonder whether at the continuous level QFS-D has the same justification as QFS-B. Although, for simplicity, Theorem 3 was phrased assuming  $\gamma_c = \partial\Omega$ , ie, for QFS-B, it easily generalizes to QFS-D by replacing  $\partial\Omega$  by  $\gamma_c$ , and noting that in the proof (18) also applies throughout the exterior of  $\gamma$ , in particular throughout the exterior of  $\Omega$  and on  $\partial\Omega$ . Theorems 26 and 27 similarly generalize.*

A rigorous justification for the discrete convergence of QFS-D, in particular the ratio (51) involving extrapolation in finite-precision arithmetic, we leave for future work.

**Remark 17 (LU, and the case of rectangular  $E$ )** *So far, for simplicity, we described the use of the SVD (57). However, partially-pivoted LU is faster for precomputation, and is still stable by Remark 5. In the square case  $P = M$ , one factorizes  $\bar{P}E = LU$ , where  $\bar{P}$  is a permutation matrix, and stores the factors and  $C$ . The apply step becomes  $\boldsymbol{\sigma} = U^{-1}(L^{-1}(\bar{P}C\boldsymbol{\tau}))$  where the parentheses and inverses indicate triangular back-substitutions done on the fly, taking  $\mathcal{O}(N^2)$  work. The Nyström matrix form (59) becomes  $\tilde{A} = (BU^{-1})(L^{-1}(\bar{P}C))$ , where inverses require back-substitutions for full stability. If  $P > M$ , as can occur when the source curve moves closer in Algorithm 1, we spectrally downsample to  $M$  source points, LU-factorize the resulting  $M \times M$  matrix, then upsample  $\boldsymbol{\sigma}$  at the end of the apply step.*

### 3.5 Tests of QFS-D for Laplace, Helmholtz, and Stokes PDEs

Now we test the desingularized method for evaluation in 2D, and study the conditioning of the resulting Nyström matrix  $\tilde{A}$ .

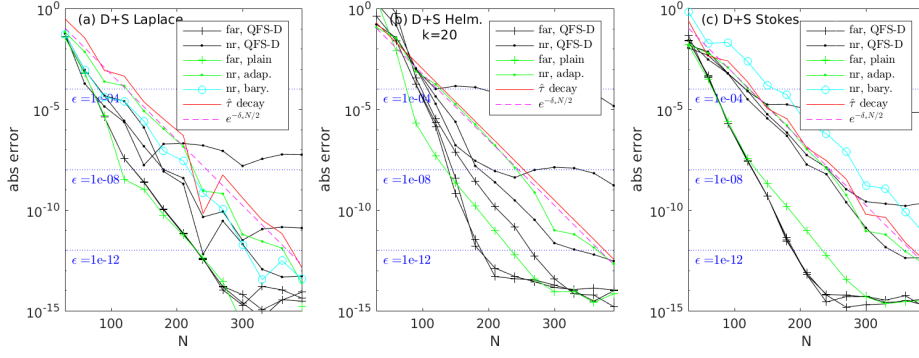


Fig. 4: Error performance of the desingularized method (QFS-D) in 2D, testing evaluation of the layer potential mixture  $\mathcal{D} + \mathcal{S}$ . All other details are as for Fig. 2.

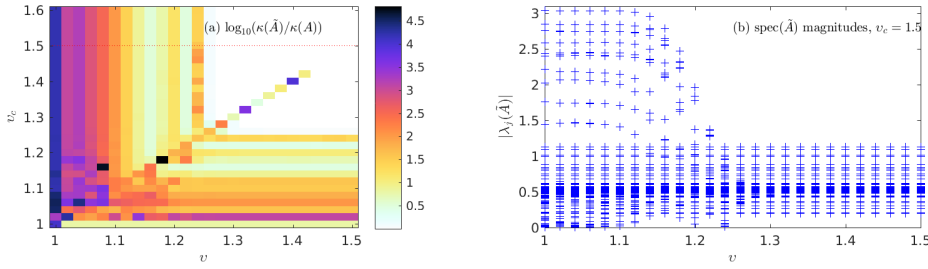


Fig. 5: Spectral properties of the QFS-D Nyström matrix  $\tilde{A}$  compared to the gold-standard Kress matrix  $A$ , discretizing the “completed” Stokes operator  $\frac{1}{2} + D + S$ . The number of nodes  $N = 200$  and tolerance  $\epsilon = 10^{-12}$  are fixed, for the star-shaped domain shown in Fig. 1. (a) shows a sweep of the condition number ratio over the source ( $v$ ) and check ( $v_c$ ) upsampling ratios. (b) shows the eigenvalue magnitudes as function of  $v$  for fixed  $v_c$ . QFS-D also internally uses the representation  $S + D$ .

Our layer-potential evaluation tests are shown in Fig. 4. They use similar set-ups to those from Sec. 3.3, with the following differences: i) we combine the desired layer potentials to test the mixture  $(\alpha, \beta) = (1, 1)$ , which is expected to follow the worse of either  $S$  or  $D$  alone; ii) in the Stokes case we choose check upsampling  $v_c = 1.5$  (recall that  $v = 1.3$  for source upsampling). For this star-shaped domain the supremum of acceptable check point distances is  $\delta_{c,0} \approx 0.09$ , controlled by its Schwarz singularities [24].

Fig. 4 shows that for all three PDEs the performance of QFS-D is better than QFS-B, sometimes exceeding the convergence rate of the gold-standard quadrature methods. A peculiar behavior for the far target is that convergence continues down to at least  $10^{-13}$  regardless of the tolerance  $\epsilon$ ; we believe this is due to the larger source-check distance  $\delta + \delta_c$ . The near target errors saturate around  $\epsilon$ , as expected. The Stokes case clearly shows that the Nyquist Fourier decay of the density controls the near-target rate for all methods, and that there is also a common rate for the far target, about twice the near rate. For Stokes, QFS-D is 1-2 digits better than the barycentric method of [9] at the near target.

The convergence of iterative methods for the linear system (5) is sensitive to the spectrum, so it is crucial that any Nyström quadrature scheme well approximate the spectral properties of the operator (4). For Laplace and Helmholtz the condition numbers are very close to those from the gold-standard Kress scheme, regardless of upsampling factors  $v \geq 1$  and  $v_c \geq 1$ , thus we recommend that both remain at 1.

However, Stokes demands upsampling, as we now show. The “completed” operator  $A = \frac{1}{2} + D + S$ , commonly used for exterior no-slip BVPs [47, 40, 11, 33, 99] is well conditioned (eg, see proof of Lemma 28). In Fig. 5(a) we compare the condition number  $\kappa(\tilde{A})$  of its Nyström matrix obtained by QFS-D to the condition number  $\kappa(A) \approx 7.2$  for  $A$  filled by Kress quadrature. The convergence (the white-colored region) of the QFS-D condition number in the  $v$  and  $v_c$  plane justifies our earlier choice of  $v = 1.3$  and  $v_c = 1.5$ . Curiously, there is a ill-conditioned “diagonal” region  $v_c \approx v$  up to about 1.42. All such behavior is believed to be due to eigenvalues of  $E$  passing through zero. Panel (b) verifies convergence of the spectrum of  $\tilde{A}$  (note the expected clustering at  $1/2$ ), showing a good, and stable, spectrum for  $v \geq 1.3$ .

To verify the correctness of  $\tilde{A}$ , we now turn to multi-body BVP applications.

## 4 Application to large-scale 2D boundary-value problems

In this section we measure the accuracy, convergence, and speed of the proposed method, in the context of FMM-accelerated algorithms for solving larger-scale BVPs. We first solve exterior Helmholtz Dirichlet (sound-hard) scattering problems with both a moderate (100) and large (1000) number of bodies. We then solve a forced Stokes flow past a moderate number of inclusions in a confined geometry. We emphasize that the same QFS method, with minimal changes, is used for both PDEs.

### 4.1 Geometry generation

For all problems presented in this section, the solution domain is the exterior of  $\Omega := \bigcup_{i=1}^K \Omega_i$ , the union of many smooth bodies. For the Stokes case only, in order to drive nontrivial flows, the solution domain will also be bounded by an enclosing circle. It is critical for testing the near-boundary layer-potential evaluations that many of the bodies are *nearly touching*, being approximately separated by a controllable distance  $d_{\min}$ . Thus in Appendix B we present a method which produces  $K$  bodies in a prescribed but random layout while insuring that:

1. all bodies are disjoint ( $\Omega_i \cap \Omega_j = \{\emptyset\}$  for  $i \neq j$ ),
2. at least some pairs of bodies have a minimum separation distance in the interval  $(d_{\min}, 1.1d_{\min}]$ , and
3. there is a controllable amount of polydispersity (variation of body size).

### 4.2 Exterior Dirichlet Helmholtz (sound-hard) scattering BVP

In this section we solve the BVP (19)–(21) in the exterior of  $\Omega$ , a collection of  $K$  smooth objects, each with boundary  $\partial\Omega_i$ . The data  $f = -u_{\text{inc}}|_{\partial\Omega}$  derives from an incident plane wave  $u_{\text{inc}}(\mathbf{x}) = e^{ik\mathbf{d}\cdot\mathbf{x}}$  with direction  $\mathbf{d} = (1, 0)$ . Once the BVP solution

$u$  is solved for, we plot the physical solution  $u_{\text{inc}} + u$ , as in the single-body example Fig. 1(a).

We use the standard indirect CFIE [57] representation (3) with mixture  $(\alpha, \beta) = (-ik, 1)$ , where  $k$  is the wavenumber, ie the 2nd-kind BIE

$$(\tfrac{1}{2} + D - ikS)\tau = f.$$

This has the  $K \times K$  block form

$$\begin{bmatrix} A^{(1,1)} & A^{(1,2)} & \dots \\ A^{(2,1)} & A^{(2,2)} & \dots \\ \vdots & \vdots & \ddots \end{bmatrix} \begin{bmatrix} \tau^{(1)} \\ \tau^{(2)} \\ \vdots \end{bmatrix} = \begin{bmatrix} f^{(1)} \\ f^{(2)} \\ \vdots \end{bmatrix}, \quad (60)$$

where the interaction operator to body  $i$  from body  $j$  is  $A^{(i,j)} = \delta_{i,j}/2 + D_{\partial\Omega_i, \partial\Omega_j} - ikS_{\partial\Omega_i, \partial\Omega_j}$ , the subscripts on operators indicating their target, source curves. We now discretize this BIE using an  $N_i$ -node periodic trapezoid rule on the  $i$ th body (postponing for now the choice of  $N_i$ ), giving  $N = \sum_{i=1}^K N_i$  total unknowns. For convenience, and without ambiguity, we also use the above notation for the discretized system.

Quadrature precomputation is as follows. We use Algorithm 1 for source and check points, but for more accuracy we add to lines 3–4 the condition that the local “speed” (magnitude of  $t$ -derivative of the function in (30)) be no less than half its corresponding value  $\|\mathbf{x}'(t)\|$  on  $\partial\Omega$ . For each body  $\Omega_i$  we independently run **QFSDprecompute** from Algorithm 2 to fill its self-interaction Nyström matrix  $A^{(i,i)}$  (from now on we drop the tilde notation). Following Remark 17 we store the LU-factors  $L^{(i)}$ ,  $U^{(i)}$  and  $\tilde{P}^{(i)}C_i$ , so that on-the-fly back-substitution is used whenever **QFSDapply** is called.

Since each body is simple and acoustically small, each  $A^{(i,i)}$  is relatively well conditioned, so a plain iterative solution of (60) is possible. However, we find that the following standard “one-body” block-diagonal preconditioning can halve the iteration count. One solves, via non-restarted GMRES [83] with prescribed tolerance, the stacked preconditioned density vector  $\tilde{\tau} := \{\tilde{\tau}^{(i)}\}_{i=1}^K$ , in

$$\begin{bmatrix} I_{N_1} & A^{(1,2)}(A^{(2,2)})^{-1} & \dots \\ A^{(2,1)}(A^{(1,1)})^{-1} & I_{N_2} & \dots \\ \vdots & \vdots & \ddots \end{bmatrix} \begin{bmatrix} \tilde{\tau}^{(1)} \\ \tilde{\tau}^{(2)} \\ \vdots \end{bmatrix} = \begin{bmatrix} f^{(1)} \\ f^{(2)} \\ \vdots \end{bmatrix}, \quad (61)$$

where  $I_{N_i}$  indicates the  $N_i \times N_i$  identity matrix. Then the density vectors on each body are recovered by  $\tau^{(i)} = (A^{(i,i)})^{-1}\tilde{\tau}^{(i)}$ . This corresponds to preconditioning (60) from the right by a matrix containing only the diagonal blocks  $(A^{(i,i)})^{-1}$ . Here, block inverses are dense and stored for later use.

What remains is to describe the FMM-accelerated *matrix-vector multiply* performed in each GMRES iteration. This applies the  $N \times N$  matrix in (61) to a vector  $\tilde{\tau}$ , as follows:

1. Split the preconditioned density  $\tilde{\tau}$  into vectors  $\tilde{\tau}^{(i)}$ .
2. Recover actual densities  $\tau^{(i)} = (A^{(i,i)})^{-1}\tilde{\tau}^{(i)}$  for each body  $i = 1, \dots, K$ .
3. Compute QFS strength vectors  $\sigma^{(i)}$  from  $\tilde{\tau}^{(i)}$  via **QFSDapply**, for each body  $i = 1, \dots, K$ .
4. Send the stack of strengths  $\{\sigma^{(i)}\}_{i=1}^K$  with corresponding QFS source locations  $\{\{\mathbf{y}_j^{(i)}\}_{j=1}^{N_i}\}_{i=1}^K$  into a single point FMM call with all  $N$  boundary nodes as targets.

Note that the Helmholtz FMM must include monopoles and dipoles scaled as in the QFS representation  $D - ikS$ .

With the iterative solution  $\tilde{\tau}$  complete, evaluation of the solution  $u$  at desired target points proceeds by doing exactly the above steps 1–4, except with the desired FMM targets instead of the boundary nodes in step 4. Complicated bookkeeping is absent (by comparison, in [8, 96], on-boundary, near-boundary, and far targets had to be handled separately).

We use a Julia implementation of Algorithm 2 that makes efficient use of a multi-core shared-memory machine, plus a custom Julia interface to the multithreaded library FMMLIB2D [31].

**Remark 18 (Sparse matrix storage of quadrature corrections to the FMM)**

*It is possible to fill a sparse matrix whose action on  $\tau$  applies all self- and close-quadrature corrections to a point FMM between boundary nodes alone [36]. One advantage of our on-the-fly approach is that storage does not grow even with many target points in the near-field. We show below that the cost it adds to the FMM is usually minor.*

We find that when there are many wavelengths across the entire system, or boundaries are close, or the number  $K$  of bodies grows, the GMRES convergence rate for (61) becomes progressively poorer. This motivates two test cases: a moderate problem (which allows detailed comparison with the Kress scheme) with  $K = 100$  quite near-to-touching inclusions solved to a high tolerance ( $10^{-12}$ ), then a larger problem with  $K = 1000$  with larger  $d_{\min}$  solved to lower tolerance ( $10^{-10}$ ). In both cases, body centers lie near two entwined spiral curves, each generated by the function  $\mathbf{r} : \mathbb{R} \rightarrow \mathbb{R}^2$ ,

$$\mathbf{r}(s) := (as + b)^p (\cos(s + \xi), \sin(s + \xi)) , \quad (62)$$

for various values  $a$ ,  $b$ , and  $p$ . The first spiral has  $\xi = 0$ , the second  $\xi = \pi$ . Each “arm” is leaky for waves, allowing partial resonance, hence keeping the iteration count tolerable.

#### 4.2.1 Computers

Throughout these examples, timing benchmarks will be measured on three computers:

1. A Macbook Pro with 16GB of RAM and a single quad-core Intel(R) Core(TM) i7-8569U CPU @ 2.80GHz,
2. A workstation with 128GB of RAM and two six-core Intel(R) Xeon(R) CPU E5-2643 v3 @ 3.40GHz,
3. A single compute node with 1TB of RAM and two AMD EPYC 7742 64-Core Processors @ 3.34GHz.

We will henceforth refer to these machines as the *Macbook*, *Workstation*, and *AMD Node*, respectively. For some of the benchmarks, we will force the computer to run all computations serially; this is done by setting the environment variables `OMP_NUM_THREADS`, `MKL_NUM_THREADS`, and `BLAS_NUM_THREADS` to 1.

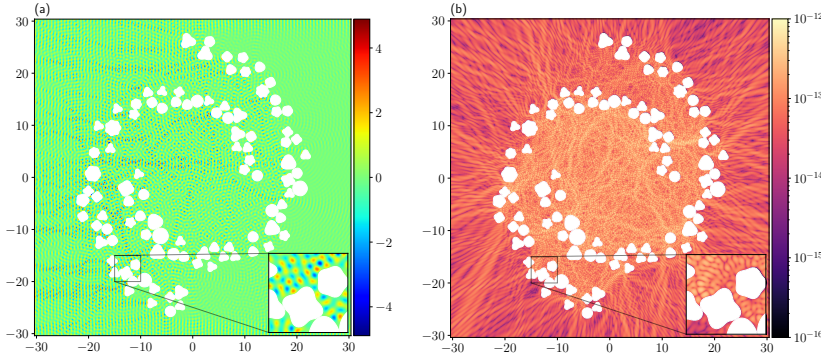


Fig. 6: Exterior Dirichlet Helmholtz scattering from 100 inclusions. (a) shows the physical solution  $u_{\text{inc}} + u$ , and (b) the absolute difference between the two finest discretizations.

#### 4.2.2 Moderately sized Helmholtz problem

We pick  $K = 100$  bodies with centers  $\mathbf{c} = \mathbf{r}(s) + \boldsymbol{\eta}$ , where  $\mathbf{r}(s)$  is the spiral (62) with parameters  $a = 3$  and  $b = p = 1$ ,  $s$  is uniform random in  $[\pi, 5\pi/2]$ , and  $\boldsymbol{\eta}$  is uniform random in  $[-1, 1]^2$ . (Specifically, this formula for  $\mathbf{c}$  acts as the `randomcenter` function in Appendix B.) The base radius is  $r_0 = 1$ , and  $d_{\min} = 0.02$ , so that the ratio of perimeter to  $d_{\min}$  (called  $f_{\text{clup}}$  in [44, 8]) is about 300. The wavenumber is  $k = 10$ ; the geometry is about 86 wavelengths across. Both the GMRES tolerance and QFS tolerance  $\epsilon$  were  $10^{-12}$ .

The baseline number  $N_i$  of quadrature nodes on the  $i$ th body is chosen such that  $2\pi R_i/N_i \approx \sqrt{d_{\min}}$ , where  $R_i$  is the maximum body radius; this is motivated by asymptotics that the smoothness scale of the density varies as the square-root of the distance between curves [85] [96, Ex. 1]. For convergence studies, larger  $N_i$  are generated simply as integer multiples of this, and the *average  $N$  per body*,  $N/K$ , is reported. The geometry and physical solution  $u_{\text{inc}} + u$  is shown in Figure 6(a).

We compare QFS to the use of Helmholtz Kress quadratures [58] on the  $N_i$  nodes, combined with plain quadrature from upsampled boundary nodes to handle nearby targets. Here boundaries are upsampled aggressively so that their target error (recalling Theorem 15) is around  $10^{-16}$ . This makes the Kress scheme very expensive, so we do not even report CPU times for it.

The absolute difference between the solution computed by the two finest discretizations is shown in Figure 6(b). Its maximum is  $6.70 \times 10^{-13}$ , less than the GMRES tolerance. A more detailed view of convergence is shown in Figure 7(a), which also compares the QFS solution to that with Kress with upsampling. The black QFS “self-convergence” curve shows the maximum ( $L^\infty$ ) difference over a  $2000 \times 2000$  grid between solutions computed at successive levels of refinement. Clearly, the convergence appears to be spectral, down to 12-digit accuracy. A much higher spectral rate is observed for the self-convergence at the (distant) target  $(0, 0)$ , both for QFS and for Kress. Their rates are indistinguishable, and furthermore converge to the same answer to 12



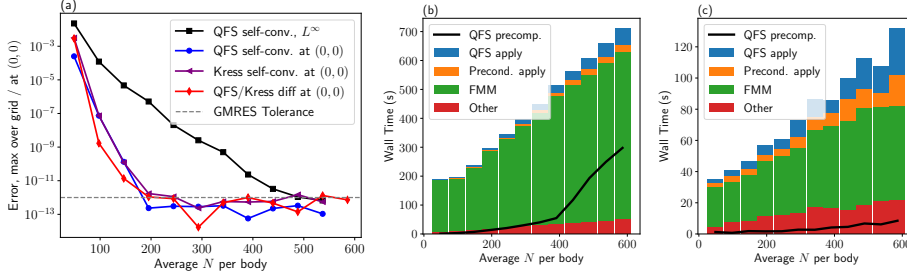


Fig. 7: Dirichlet Helmholtz scattering problem with 100 inclusions. (a) shows convergence of the proposed QFS scheme at a similar rate to that of gold-standard Kress quadratures plus expensive upsampling. CPU timings are shown in (b) and (c) on the Macbook and AMD Node, respectively (see Section 4.2.2).

digits (red curve). (We note that Kress, even with upsampling, is unable to accurately evaluate on all of the grid points used for  $L^\infty$ -norm testing of QFS.)

Finally, in Figure 7(b) and (c), we show wall-clock times for these simulations on the Macbook and AMD Node, respectively. The black line shows the QFS precomputation time, which includes the time required to form and invert the Nystrom matrices  $A^{(i,i)}$ . Bars show the total time (accumulated over all GMRES iterations) for **QFSDapply** routine (blue), the block-diagonal preconditioner (orange), and the point FMM (green). The red block shows all time not accounted for by these processes, which is dominated by internals of GMRES. Although the percentage of the total solve time consumed by **QFSDapply** grows as  $N$  does, it never exceeds 8% or 25% on the Macbook and the AMD Node, respectively. In fact, for this high-iteration count problem, the time used by orthogonalization within GMRES is similar to that used by QFS for quadrature, especially as the thread-count over which the FMM and the **QFSDapply** routines can be split increases. A tabulation of results is presented in Table 1. For all discretizations for both methods, the iteration count for GMRES to converge to  $10^{-12}$  is exactly 854.

**Remark 19 (Optimizations for repeated objects)** *The timing results presented here are actually a worst-case scenario: all of the scattering surfaces are unique so need their own QFS precomputation. If objects repeat, two optimizations appear: (1) the **QFSDprecompute** stage needs to be done only once for each unique object, and (2), because the matrices appearing in the **QFSDapply** algorithm are the same, all steps in Algorithm 2 can be packed together into highly-optimized BLAS3/LAPACK calls. These optimizations are possible for the QFS-B algorithm, as well.*

#### 4.2.3 Large Helmholtz problem

We repeat the tests from the previous section, with  $K = 1000$  obstacles and spiral parameters  $a = 4$ ,  $b = 7$  and  $p = 1.4$ , with  $s$  in (62) uniform random in  $[\pi, 7\pi/2]$ , and  $\mathbf{c} = \mathbf{r}(s) + \boldsymbol{\eta}$ , but now  $\boldsymbol{\eta}$  is uniform random in  $[-2, 2]^2$ . We set  $\delta = 0.05$ , two and a half times larger than before. The GMRES and QFS tolerances are  $10^{-10}$ . The wavenumber is  $k = 1$ , giving about 76 wavelengths across; see Figure 8(a).

Average $N$ per body	49	147	244	342	439	537
GMRES Iter., QFS	854	854	854	854	854	854
GMRES Iter., Kress	854	854	854	854	854	854
Self-conv., $L^\infty$	2.3e-2	4.7e-6	2.0e-8	5.0e-10	3.3e-12	6.7e-13
Self-conv., $(0, 0)$	2.5e-4	1.3e-10	3.0e-13	3.3e-13	2.2e-13	1.0e-13
Kress/QFS Diff	2.9e-3	1.3e-11	1.1e-12	4.6e-13	5.2e-13	8.3e-13
Timing (in seconds, Macbook)						
QFS Precomp.	0.9	7.1	20.5	40.1	117.2	249.5
QFS Apply	1.5	5.4	12.0	21.3	33.3	48.9
Precond. apply	0.6	2.2	5.5	9.3	15.0	22.1
FMM	181.9	216.8	307.1	389.8	479.7	544.3
Other	6.7	10.1	16.1	16.7	20.3	23.5
Total Solve	187.7	236.4	344.8	448.4	564.2	660.2
QFS % of Total	0.8	2.3	3.5	4.8	5.9	7.4

Table 1: Tabulation of the results from the moderately size Helmholtz problem from Section 4.2.2. See discussion and Figures 6 and 7 for further analysis.

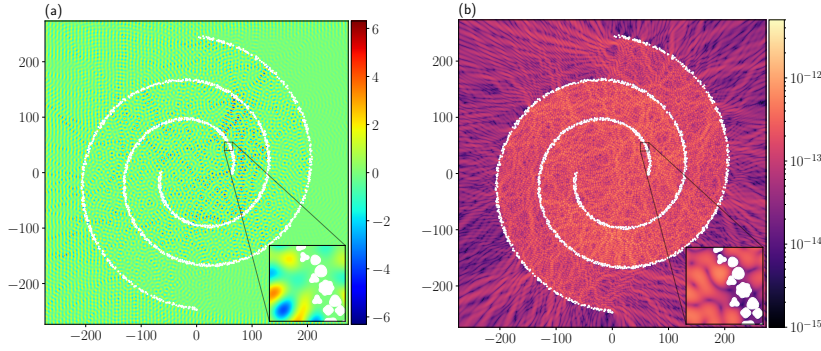


Fig. 8: Exterior Dirichlet Helmholtz scattering from 1000 inclusions. (a) shows the physical solution  $u_{\text{inc}} + u$ , and (b) the absolute difference between the two finest discretizations.

As in Section 4.2.2, we measure self-convergence in  $L^\infty$  and at the far field point  $(0, 0)$ , but do not compare to a Kress-based solver due to computational cost. A self-convergence study is shown in Figure 9(a), consistent with a spectral rate, with convergence stagnating below the GMRES tolerance for both near and far targets. Timings on the AMD Node are shown in Figure 9(b). As before, the `QFSDapply` stage consumes a small portion of the total solve time ( $< 22\%$ ). A tabulation of all results is presented in Table 2.

#### 4.3 Driven Stokes flow in 2D

In this section we consider pressure-driven Stokes flow past a fixed array of obstacles. The centers for the individual obstacles are drawn by rejection sampling  $\mathbf{c}$  uniformly

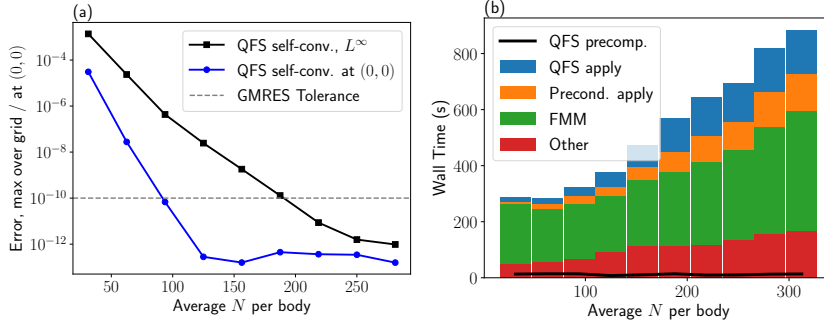


Fig. 9: Exterior Dirichlet Helmholtz scattering problem with 1000 inclusions. Panel (a) shows self-convergence results, both maximum over the grid (black) and at (0,0) (blue). Panel (b) shows computational timings.

Average $N$ per body	31	94	156	219	281
GMRES Iterations	1331	1331	1331	1331	1331
Self-conv., $L^\infty$	1.4e-3	4.3e-7	1.8e-9	8.6e-12	9.7e-13
Self-conv., (0,0)	3.1e-5	6.8e-11	1.6e-13	3.6e-13	1.6e-13
Timing (in seconds, AMD Node)					
QFS Precomp.	13.2	14.1	10.6	9.6	12.9
QFS Apply	16.0	33.8	79.3	140.1	155.3
Precond. apply	9.5	27.5	45.7	93.2	125.2
FMM	210.1	196.7	237.6	296.5	381.6
Other	49.5	66.4	111.4	114.9	156.2
Total Solve	285.8	324.4	474.0	645.3	818.2
QFS % of Total	5.6	10.4	16.7	21.8	18.9

Table 2: Tabulation of the results from the large Helmholtz problem from Section 4.2.3.

in  $[-15, 15]^2$ , discarding those with  $|\mathbf{c}| > 14 - d_{\min}$ , with  $d_{\min} = 0.05$ , and geometry generation otherwise proceeds as described in Appendix B, with the additional stipulation that no part of any obstacle curve can lie within  $d_{\min}$  of an outer confining ring of radius 15. The flow is forced by fixing constant  $\mathbf{u} = (1, 0)$  velocity (Dirichlet) data on the outer boundary; a no slip condition ( $\mathbf{u} = \mathbf{0}$ ) is enforced at all inner obstacles. This differs from (23)–(25) only in that the domain is bounded, removing the decay condition. The solution  $(\mathbf{u}, p)$  is then unique up to a constant in  $p$ . Figure 10 shows the geometry.

We use the completed formulation  $\mathcal{D} + \mathcal{S}$  on each body, which is proven to remove their nullspaces [47] [79, p.50]. On the outer circle, denoted by  $\partial\Omega_0$ , we use a plain DLP, but perturb the self-interaction of that block with a rank-1 operator  $\mathbf{nn}^\top$ , where  $\mathbf{n}$  in the unit normal. This removes the 1D nullspace associated with the interior BVP [46, Table 2.3.4] [11]. With  $j = 1, \dots, K$  indexing the interior obstacles, the BIE takes the  $(K+1) \times (K+1)$  block form

$$\begin{bmatrix} -\frac{1}{2} + D_{\partial\Omega_0, \partial\Omega_0} + \mathbf{nn}^\top & D_{\partial\Omega_0, \partial\Omega_1} + S_{\partial\Omega_0, \partial\Omega_1} & \dots \\ D_{\partial\Omega_1, \partial\Omega_0} & \frac{1}{2} + D_{\partial\Omega_1, \partial\Omega_1} + S_{\partial\Omega_1, \partial\Omega_1} & \dots \\ \vdots & \vdots & \ddots \end{bmatrix} \begin{bmatrix} \boldsymbol{\tau}^{(0)} \\ \boldsymbol{\tau}^{(1)} \\ \vdots \end{bmatrix} = \begin{bmatrix} \mathbf{f}^{(0)} \\ \mathbf{f}^{(1)} \\ \vdots \end{bmatrix}. \quad (63)$$

Each boundary is discretized with the PTR as for Helmholtz in Section 4.2, giving  $N = 2 \left( N_{\text{circ}} + \sum_{i=1}^K N_i \right)$  total unknowns. The discretization of  $\mathbf{nn}^\top$  is as in Remark 21. The QFS mixture becomes  $(\tilde{\alpha}, \tilde{\beta}) = (1, 1)$ , proven to be robust for Stokes in Theorem 27. Other than this, the use of QFS-D is almost identical to the Helmholtz case, a key advantage of the scheme.

A couple of remarks are in order, mostly relating to the new enclosing boundary and pressure evaluation.

**Remark 20 (Circular boundaries)** *In the special case of a circular boundary, the “check from source”, “check from boundary”, and “boundary from source” matrices  $E$ ,  $C$ , and  $B$  are circulant (immediately for scalar PDEs, and so long as expressed in a polar coordinate system for vector PDEs). Thus for  $N_{\text{circ}}$  large, the circulant property may be exploited via FFTs to stably apply and invert  $D_{\partial\Omega_0, \partial\Omega_0}$ .*

**Remark 21 (Rank-deficiency removal for interior Stokes QFS)** *We use QFS on the confining boundary  $\partial\Omega_0$  by negating  $\delta$  and  $\delta_c$  for interior evaluation. The “check from source” matrix  $E$  now must have a 1D null-space associated with the pressure constant ambiguity. Although this can be dealt with by regularizing the SVD (57), we prefer to use a low-rank perturbation to remove rank deficiency. We replace  $E$  by*

$$E_{\text{augmented}} = E + \mathbf{n}_{\text{check}}(w_{\text{source}}\mathbf{n}_{\text{source}})^\top, \quad (64)$$

where  $w_{\text{source}}$  elementwise-multiplies by arc-length quadrature weights for the source curve  $\gamma$ , and  $\mathbf{n}$  indicates a column-vector of normals at source or check points.

**Remark 22 (QFS for pressure evaluation)** *The kernels (27)–(28) are for velocity  $\mathbf{u}$  evaluation. With  $\tau$  solved for in (63), the pressure solution  $p$  may also be evaluated via the associated 2D pressure kernels [62] [46, Sec. 2.3]*

$$G_p(\mathbf{x}, \mathbf{y}) = \frac{1}{2\pi} \frac{\mathbf{r}}{r^2}, \quad D_p(\mathbf{x}, \mathbf{y}) = \frac{\mu}{\pi} \left( -\frac{\mathbf{ny}}{r^2} + 2(\mathbf{r} \cdot \mathbf{ny}) \frac{\mathbf{r}}{r^4} \right), \quad \mathbf{r} := \mathbf{x} - \mathbf{y}, \quad r := \|\mathbf{r}\| \quad (65)$$

with the QFS source strengths  $\sigma$ , analogous to (11). Since the interior BVP solution is only defined up to a pressure constant, we are done.

However, a more general requirement is that QFS evaluate  $p$  with the correct constant. This is guaranteed in exterior QFS, because both the desired representation (3) and QFS source representation have pressures vanishing as  $r \rightarrow \infty$ , simply because the kernels (65) do. For interior QFS evaluation the collocation of  $\mathbf{u}$  on  $\gamma_c$  leaves  $p$  generally off by a constant. To fix this we compute the  $p$  difference relative to plain quadrature at a far-field point, then add this difference as a multiple of  $\mathbf{n}_{\text{source}}$  to the QFS source strengths. This corrects  $p$  but leaves  $\mathbf{u}$  unaffected.

The density  $\tau$  is found by solving Equation (63) using one-body right-preconditioned GMRES to a tolerance of  $10^{-9}$ , as in Section 4.2. Figure 10 shows the resulting solution  $(\mathbf{u}, p)$  evaluated by QFS. Forcing the flow through these tightly packed obstacles requires an enormous pressure gradient, and large flows avoid the narrowest constrictions, instead rushing through the widest contiguous paths. The pointwise difference in  $u/\|\mathbf{u}\|_{L^\infty}$  between the two finest resolutions is shown in panel (c); the largest difference is  $8.7 \times 10^{-11}$ .

The convergence with respect to the mean value of  $N_i$  appears spectral in Figure 11(a), with a faster far-field rate than in the near-field. We compare QFS again to

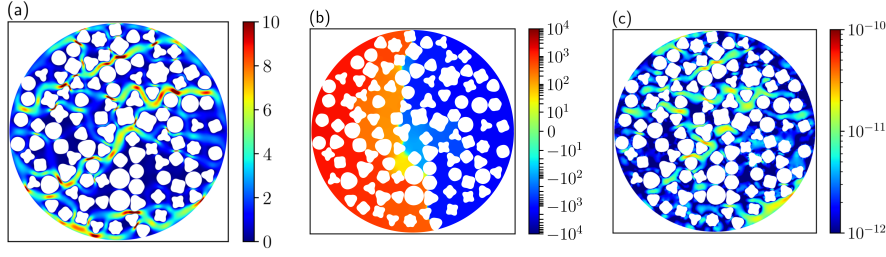


Fig. 10: Driven Stokes flow around 100 no-slip inclusions. Panels (a) and (b) show the speed  $|\mathbf{u}|$  and pressure  $p$ , respectively, computed at the finest discretization. Panel (c) shows the estimated error in  $u$ , normalized by  $\|\mathbf{u}\|_{L^\infty}$ .

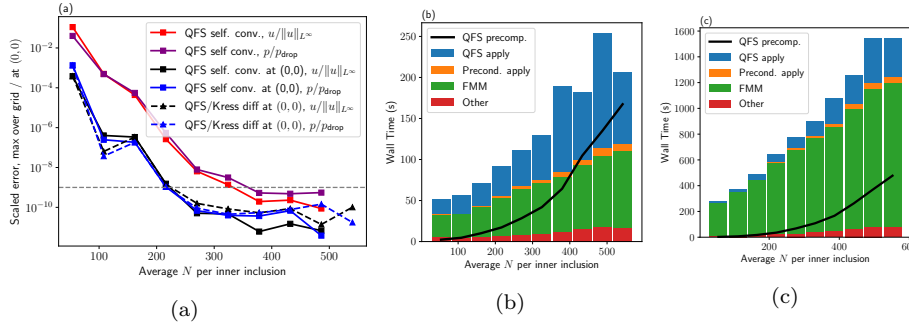


Fig. 11: Driven 2D Stokes flow past 100 inclusions. Panel (a) shows the self-convergence of QFS (measured both over a grid and at only a far-field point) and the difference between the QFS solution and gold-standard Kress solution at a far-field point. Errors in  $u$  are normalized by  $\|\mathbf{u}\|_{L^\infty}$ ; errors in  $p$  are normalized by  $p_{\text{drop}}$ , the maximal pressure drop over the domain. Panels (b) and (c) show computational timings on the Workstation; using all cores (b) or in serial (c).

the Kress quadratures (which apply to the log-singular  $S$  operator): for both  $\mathbf{u}$  and  $p$ , they converge rapidly to one another at a far-field point.

Figure 11(b) shows timings on the Workstation, using all 12 cores. Unlike for our Helmholtz implementation, the `QFSDapply` routine often uses a large percentage of the compute time. The Stokes code used here is based on an older Python implementation that uses an unthreaded loop over the bodies, relying on BLAS for parallelization, which gives poor scaling when solving many small-sized problems. In contrast, we use a wrapper to a Fortran biharmonic 2D FMM [79] that scales well across processors, leaving the `QFSDapply` stage to dominate the computation. Note that since  $\nu = 1.3$ , the FMM involves about  $1.3N$  sources and  $N$  targets. Panel (c) shows timings on the same computer, forced to run in serial; now the `QFSDapply` stage takes no more than 23% of the total time for any discretization. These serial results are collected in Table 3. For very sparse discretizations, QFS uses slightly more iterations than Kress (592 vs. 571), but the differences disappear upon refinement.

Average $N$ per body	54	162	270	378	486
GMRES Iterations, QFS	592	571	570	573	570
GMRES Iterations, Kress	571	578	570	570	571
Convergence for $u/\ u\ _{L^\infty}$					
Self-conv., $L^\infty$	1.1e-1	4.4e-5	6.4e-9	2.0e-10	8.7e-11
Self-conv., (0, 0)	3.8e-4	3.4e-7	5.0e-11	6.1e-12	6.8e-12
QFS/Kress diff, (0, 0)	3.8e-4	3.4e-7	1.6e-10	5.3e-11	1.4e-11
Convergence for $p/p_{\text{drop}}$					
Self-conv., $L^\infty$	4.9e-2	5.54e-5	7.9e-9	5.3e-10	5.5e-10
Self-conv., (0, 0)	1.3e-3	1.8e-7	6.8e-11	3.7e-11	3.8e-12
QFS/Kress diff, (0, 0)	1.3e-4	1.8e-7	9.1e-11	5.4e-11	1.4e-10
Timing (in seconds, Workstation, serial)					
QFS Precomp.	2.4	17.7	67.9	166.5	371.6
QFS Apply	14.9	40.1	84.2	196.3	348.7
Precond. apply	0.9	5.4	11.4	22.3	43.4
FMM	259.2	424.0	651.4	814.4	1072.3
Other	4.2	14.9	26.6	44.0	78.3
Total Solve	279.2	484.4	773.6	1077.0	1542.3
QFS % of Total	5.3	8.3	10.9	18.2	22.6

Table 3: Tabulation of the results from the Stokes problem from Section 4.3. See discussion and Figures 10 and 11 for further analysis.

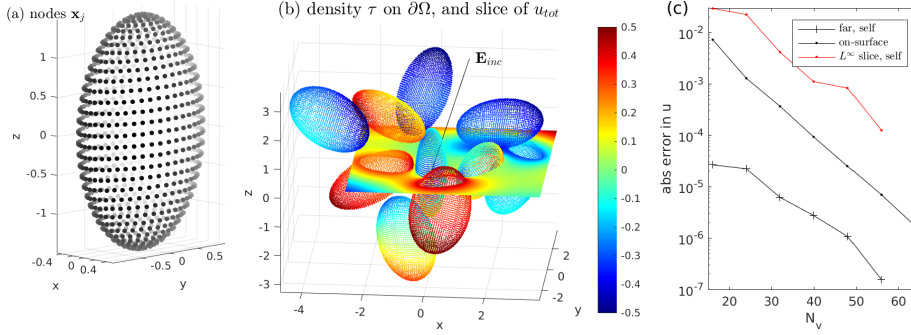


Fig. 12: 3D Exterior Laplace BVP example for  $K = 10$  triaxial ellipsoids, with minimum separations  $d_{\min} = 0.1$ , solved and evaluated with QFS-D. (a) shows the  $N_0 = 1408$  surface nodes for the resolution  $N_v = 32$ . (b) shows the physical potential  $u_{\text{tot}}$  (using the colorscale) on a slice  $z \approx 0.192$ , and density  $\tau$  (multiplied by 0.3 to fit the same colorscale), for  $N_v = 64$ . (c) shows convergence of the solution potential  $u$  at various points. At the highest  $N_v = 64$ , there are  $N = 36040$  total degrees of freedom.

## 5 Laplace 3D implementation and test

We now describe a preliminary dense (non-accelerated) test of QFS-D in the exterior of several identical ellipsoids of semiaxes  $(1/2, 1, 3/2)$ , ie, aspect ratio 3. Since the ellipsoid is triaxial, quadrature techniques for bodies of revolution (eg [2, 64]) do not apply.

We “grew” a cluster  $\Omega$  of  $K = 10$  such ellipsoids, each a distance  $d_{\min} = 0.1$  from at least one other, as follows: for each new body, after choosing a random orientation

in  $\text{SO}(3)$ , we translate it along a line with random orientation pointing towards  $\mathbf{0}$  until the minimum distance to any other body approximates  $d_{\min}$  to  $10^{-6}$ .<sup>1</sup> We model an electrostatics problem where the  $j$ th conducting body has constant voltage  $V_j$  (chosen at random in  $[-\frac{1}{2}, \frac{1}{2}]$ ), plus there is an applied electric field  $\mathbf{E}_{\text{inc}}$  (with strength 0.3 in the direction shown in Fig. 12(b), imposing a voltage drop of 2.25 across the cluster). The physical potential is  $u_{\text{tot}} = u_{\text{inc}} + u$ , where  $u_{\text{inc}}(\mathbf{x}) = \mathbf{E}_{\text{inc}} \cdot \mathbf{x}$ , whereas  $u$  solves the  $d = 3$  Laplace BVP (12)–(14) with data on the  $j$ th boundary  $f_j(\mathbf{x}) = V_j - u_{\text{inc}}(\mathbf{x})$ ,  $\mathbf{x} \in \partial\Omega_j$ .

We use the completed representation  $u = (\mathcal{D} + S)\tau$  in  $\mathbb{R}^3 \setminus \overline{\Omega}$ , leading to the well-conditioned BIE

$$(\tfrac{1}{2} + D + S)\tau = f,$$

which we discretize via QFS-D as follows. The ellipsoid (axis-aligned at the origin) is parameterized  $\mathbf{r}(u, v) = (\sqrt{1-v^2}\cos u)/2, \sqrt{1-v^2}\sin u, 3v/2)$ , for  $(u, v) \in [0, 2\pi] \times [-1, 1]$ . Our spectrally-accurate global surface quadrature is controlled by  $N_v$ , the number of Gauss-Legendre nodes  $v_j$  covering  $v \in [-1, 1]$ . On each loop  $v = v_j$  we place an  $n_j$ -node periodic trapezoid rule in  $u$ , where  $n_j$  is the smallest even number larger than  $\min[(4N_v/3)(1-v_j^2)^{1/2}, 8]$ . This scales  $n_j$  by the loop circumference to uniformize the node density. Weights are the products of the 1D rule weights and the Jacobian  $\|\mathbf{r}_u \times \mathbf{r}_v\|$ . There are about  $N_0 = 0.9N_v^2$  nodes on the ellipsoid; see Fig. 12(a).

QFS sources are located by simple constant normal displacement without upsampling:  $\mathbf{y}_j = \mathbf{x}_j - \delta \mathbf{n}_j$ , where  $\delta = 0.08$  (somewhat below the smallest radius of curvature) was chosen by experiment. Similarly, the exterior check points are  $\mathbf{z}_j = \mathbf{x}_j + \delta_c \mathbf{n}_j$  with  $\delta_c = 0.01$ . We chose an upsampling factor  $\rho = 3$ , sufficient for around 9 digits of accuracy at check points.

The only missing ingredient is a spectral upsampling matrix  $L_{\tilde{N} \times N}$  that maps values at nodes from a  $N$ -node rule controlled by  $N_v$  to an  $\tilde{N}$ -node rule controlled by  $\tilde{N}_v = \rho N_v$ . In brief this applies length- $n_j$  1D discrete Fourier transforms (DFTs) on the  $j$ th loop, zero-pads all modes up to the frequency  $\max_j n_j/2$ , applies barycentric Lagrange interpolation onto new nodes in the  $v$  direction (separately for each Fourier mode), then applies zero-padded length- $\tilde{n}_j$  inverse 1D DFTs to recover values on the  $j$ th output loop. In practice this is a chain of matrix-matrix or Kronecker products. A subtlety is that for odd modes only, the Lagrange interpolation must be performed on the function divided by  $\sqrt{1-v^2}$ , recalling that associated Legendre functions  $P_n^m(v)$  with odd  $m$  are polynomials in  $v$  multiplied by this factor [4, Sec. 12.5]. Our code to fill  $L_{\tilde{N} \times N}$  is about 30 lines of MATLAB.

We now have all the QFS-D pieces, so use Algorithm 2 (LU variant as in Remark 17) to precompute  $L$ ,  $U$  and  $\bar{P}C$ , using the  $d = 3$  Laplace kernel (15) and the pure SLP  $(\tilde{\alpha}, \tilde{\beta}) = (1, 0)$  QFS mixture. Since we do not seek accuracies near  $\epsilon_{\text{mach}}$ , we simply store  $X = U^{-1}(L^{-1}(\bar{P}C))$  then get the  $N_0 \times N_0$  1-body Nyström matrix  $A_0 = BX$ .

**Remark 23** *The spectrum of  $A_0$  may be improved by two-sided averaging [56, 72]:  $A_0$  becomes the average of interior and exterior QFS discretizations, with the  $I/2$  jump term then added explicitly. This gives  $\kappa(A_0) \in [2.5, 2.9]$  for all resolutions tested.*

The dense  $KN_0 \times KN_0$  Nyström matrix  $A$  is now filled with  $A_0$  as diagonal blocks, and offdiagonal blocks  $A^{(i,j)} = B^{(i,j)}X$ , where  $B^{(i,j)}$  is a matrix evaluating the SLP kernel  $G$  from the QFS source locations for body  $j$  to the nodes of body  $i$ .

<sup>1</sup> The distance between any two ellipsoids is found by alternating projection, with each projection using a Newton iteration for a Lagrange multiplier.



GMRES with tolerance  $10^{-8}$  is used with dense matrix-vector multiplication, requiring exactly 24 iterations for all resolutions tested, apart from the smallest  $N_v = 16$ . Thus we do not use one-body preconditioning. The density  $\tau$  solving the linear system is shown in Fig. 12(b).

The convergence of various errors in  $u$  with  $N_v$  is shown by Fig. 12(c), and appears to be spectral. At a “far” target ( $\mathbf{x} = (1, -1, 2)$ , a distance 1.15 from the nearest body), 7-digit accuracy is reached by  $N_v = 56$ , or  $N_0 = 2792$  per body, estimated by self-convergence. At a generic on-surface target on body  $j = 1$  the value of  $u_{\text{tot}} - V_1$  (and hence the error, shown with black dots), reaches close to 6-digit accuracy at  $N_v = 64$ . A tougher test is the  $L^\infty$  error over a 2D slice of 54246 exterior targets (see Fig. 12(b)) with grid spacing 0.025, and passing through at least one nearest-touching point, and including a target  $2 \times 10^{-5}$  from one of the bodies. Shown by the red curve, this reaches only 4-digit accuracy at  $N_v = 56$ , although the rate seems the same. As expected, the worst errors occur at near-touching regions and are oscillatory at the node scale.

**Remark 24** *Out of curiosity we have made this BVP challenging by imposing  $\mathcal{O}(1)$  voltage differences between bodies, resulting in large fields  $\|\nabla u\| \approx 10$ , and density near-singularities at close-touching points. This may be analogous to velocity differences that occur in Stokes with rigid bodies [80, 20, 96]. With the same  $u_{\text{inc}}$ , if we set all  $V_j = 0$ , the BVP becomes easier, the densities nonsingular, and all  $L^\infty$  and on-surface errors improve by at least 1 digit.*

Even though our implementation was naive, using a dense  $A$ , timings were reasonable. We worked in MATLAB on a laptop with a quad-core Intel i7-7700HQ CPU and 32 GB RAM. At  $N_v = 40$  (giving uniform 3-digit accuracy), the entire calculation is done in 11 seconds. At the largest  $N_v = 64$ , two-sided QFS-D took 30 s to fill  $A_0$  (dominated by wielding  $L_{\tilde{N} \times N}$ ), 70 s to fill  $A$ , and 14 s for its GMRES solution. Storing this  $A$  needs 10 GB; obviously an FMM-accelerated version would not have this limitation. New densities can be converted into QFS source strengths at a rate of at least  $10^6$  points/s; this would enable a 3D FMM to perform accurate evaluations close to or on surfaces with little extra cost.

## 6 Conclusions

We have explored in depth, analytically and numerically, a proposal to use an *effective source representation* for the efficient spectrally-accurate evaluation of layer potentials living on simple curves and surfaces. The map to source strengths is precomputed by *collocation* either on the boundary (QFS-B) or on a nearby “check boundary” (QFS-D). The latter needs only a family of *smooth* quadratures on  $\partial\Omega$ , and a high-order upsampling (interpolation) rule between members of the family. We show that, with 2D periodic trapezoid nodes, error performance is similar to the best-known schemes: Kress for on-surface and expensive adaptive quadrature for off-surface. We expect it to add to the toolkit for large-scale simulations in complex media, including viscous flows, wave scattering, electrostatics (three cases we study here), as well as sedimentation, vesicle dynamics, Maxwell, elastostatics, and elastodynamics.

The counterintuitive underlying idea—solving an ill-conditioned 1st-kind integral equation to give a new global evaluator for a well-conditioned 2nd-kind integral equation—brings several advantages: distant, near, and on-surface targets all use the *same* accurate representation (making acceleration almost trivial, given a point-FMM code),

singular quadratures are replaced with an upsampled smooth rule (as in QBX [56,6] or hedgehog [72]), and the method is kernel-independent, allowing easy implementations for various scalar and vector PDEs.

Our scheme is efficient when there are many simple bodies. This hangs on the philosophy that *it is worth spending a lot of effort to create a good layer-potential representation that will be reused a huge number of times (GMRES iterations, simulation time-steps, etc)*. Since the idea is essentially a precomputed solution operator for the method of fundamental solutions (MFS), it comes with the same caveats about the shape as the MFS. While even 2D corners can be handled by the MFS [45,68,34], in 3D there is probably a limitation to simple smooth bodies.

On the theory side, we proved robustness (assuming potential value collocation on the check curve), showing that general conditions (C1-C2) hold for three common PDEs, in 2D and 3D, for sufficiently analytic data. Our discrete analysis in 2D invoked MFS and BIE literature, but aspects such as the ratio condition (51) seem more difficult to analyze.

**Remark 25 (Why not just use MFS?)** *Given the success of 1st-kind representations “under the hood” of QFS, the reader may wonder whether one should just instead use (one-body preconditioned) MFS to solve the entire multi-body BVP. Such a method has utility (eg [67]). However, this would not fit within our goal of providing a general black-box layer-potential evaluator tool.*

Future work suggested by this study includes i) application to Neumann and other boundary conditions, ii) FMM-accelerated 3D mobility solvers, and iii) clustered MFS source locations to handle corner domains [45,68,34]. There also remain interesting analysis questions such as understanding upsampling factors for 2D Stokes on the disk.

**Acknowledgements** We are grateful for discussions with Manas Rachh, and the use of his 2D biharmonic FMM code. We thank Ralf Hiptmair for asking a question (along the lines of “why can’t interior multipoles be used to precompute a quadrature for a rigid object?”) at an ICOSAHOM 2018 talk that helped inspire this work. The Flatiron Institute is a division of the Simons Foundation.

## A Robustness of continuous QFS representations for analytic data in three PDEs

Here we prove Theorem 3, then state and prove versions for Helmholtz and Stokes, which need adjustments. We use ideas from Doicu–Eremin–Wriedt [25, Ch. IV, Thms. 2.1-2], who considered the only the pure SLP for Helmholtz. These theorems are thus also useful for any MFS (first-kind IE) method for exterior BVPs.

We consider  $\Omega \subset \mathbb{R}^d$  with smooth boundary  $\partial\Omega$ , and  $\gamma \subset \Omega$  a smooth simple closed source curve (in  $d = 2$ ) or source surface ( $d = 3$ ), enclosing a domain  $\Omega_- \subset \Omega$ . We abbreviate  $u_{\mathbf{n}} := \partial u / \partial \mathbf{n}$ .

*Proof (Proof of Theorem 3.)* Using  $u$  to also denote the continuation of the solution, one may read off its data on  $\gamma$ , and the exterior Green’s representation formula [46, (1.4.5)] holds,

$$u(\mathbf{x}) = \int_{\gamma} \left[ -G(\mathbf{x}, \mathbf{y}) u_{\mathbf{n}}(\mathbf{y}) + \frac{\partial G(\mathbf{x}, \mathbf{y})}{\partial \mathbf{n}_{\mathbf{y}}} u(\mathbf{y}) \right] ds_{\mathbf{y}}, \quad \mathbf{x} \in \mathbb{R}^d \setminus \overline{\Omega_-}. \quad (66)$$

Note that, by the decay condition, no constant term is needed. Let  $v$  be the unique solution to the Laplace BVP interior to  $\gamma$  with Dirichlet data  $v = u$  on  $\gamma$ , then let  $v_{\mathbf{n}}^-$  be its normal

derivative, then the exterior extinction GRF holds

$$0 = \int_{\gamma} \left[ G(\mathbf{x}, \mathbf{y}) v_{\mathbf{n}}^{-}(\mathbf{y}) - \frac{\partial G(\mathbf{x}, \mathbf{y})}{\partial \mathbf{n}_{\mathbf{y}}} v(\mathbf{y}) \right] d\mathbf{s}_{\mathbf{y}}, \quad \mathbf{x} \in \mathbb{R}^d \setminus \overline{\Omega_-}. \quad (67)$$

Adding the last two equations cancels the DLP terms, leaving (18) with

$$\sigma(\mathbf{y}) := v_{\mathbf{n}}^{-}(\mathbf{y}) - u_{\mathbf{n}}(\mathbf{y}), \quad \mathbf{y} \in \gamma,$$

a density solving (17). Since all data on  $\gamma$  was analytic,  $\sigma$  is certainly smooth.

For uniqueness, instead let  $\sigma$  solve (17) with zero RHS. Construct  $u$  via (18) from this  $\sigma$ , then  $u$  vanishes on  $\partial\Omega$  by the uniqueness of the exterior Dirichlet BVP in  $d = 3$ , or by Lemma 2 in  $d = 2$ ,  $u \equiv 0$  in  $\mathbb{R}^d \setminus \Omega$ . By unique continuation from Cauchy data  $u \equiv u_n \equiv 0$  on  $\partial\Omega$ ,  $u$  vanishes also in  $\mathbb{R}^d \setminus \overline{\Omega_-}$ . Since the potential is continuous across a single-layer [59, Thm. 6.14], and  $u$  is harmonic in  $\Omega_-$ , then  $u$  solves the interior Dirichlet BVP in  $\Omega_-$  with vanishing data. By uniqueness of this BVP,  $u$  vanishes in  $\Omega_-$ , thus both limits of  $u_{\mathbf{n}}$  either side of  $\gamma$  vanish, so by the jump relation [59, Thm. 6.18],  $\sigma \equiv 0$ .

We now state and prove variants for the other two PDEs tested in this work.

**Theorem 26 (QFS robustness for exterior Helmholtz)** *Let  $u$  solve (19) and (21) for  $k > 0$ , with  $u = u_c$  on  $\partial\Omega$ . Let  $u$  also continue as a Helmholtz solution throughout the closed annulus (or shell) between  $\partial\Omega$  and a simple smooth interior surface  $\gamma \subset \Omega$ . Let  $\eta \in \mathbb{R}$ ,  $\eta \neq 0$ . Let  $G$  be the fundamental solution (22). Then the first kind combined-field integral equation*

$$\int_{\gamma} \left[ \frac{\partial G(\mathbf{x}, \mathbf{y})}{\partial \mathbf{n}_{\mathbf{y}}} - i\eta G(\mathbf{x}, \mathbf{y}) \right] \sigma(\mathbf{y}) d\mathbf{s}_{\mathbf{y}} = u_c(\mathbf{x}), \quad \mathbf{x} \in \partial\Omega \quad (68)$$

has a unique solution  $\sigma \in C^\infty(\gamma)$ , and

$$u(\mathbf{x}) = \int_{\gamma} \left[ \frac{\partial G(\mathbf{x}, \mathbf{y})}{\partial \mathbf{n}_{\mathbf{y}}} - i\eta G(\mathbf{x}, \mathbf{y}) \right] \sigma(\mathbf{y}) d\mathbf{s}_{\mathbf{y}}, \quad \mathbf{x} \in \Omega \setminus \mathbb{R}^d. \quad (69)$$

*Proof* We use  $u$  to denote the continuation of  $u$  as a Helmholtz solution onto  $\gamma$ . Let  $v$  solve the homogeneous Helmholtz impedance BVP in the interior of  $\gamma$ , with boundary data

$$v_{\mathbf{n}} - i\eta v = u_{\mathbf{n}} - i\eta u \quad \text{on } \gamma. \quad (70)$$

It is standard that this BVP has a unique solution for any real  $k$  [86, Sec. 8.8] (or [30, Prop 2.1]). Adding the Helmholtz versions of the GRFs (66) (which applies since  $u$  is radiative [19, Sec. 2.2]) and (67), and adding and subtracting  $i\eta(v - u)$ , we get

$$u(\mathbf{x}) = \int_{\gamma} \left[ G(\mathbf{x}, \mathbf{y}) [v_{\mathbf{n}} - i\eta v - (u_{\mathbf{n}} - i\eta u) + i\eta(v - u)] - \frac{\partial G(\mathbf{x}, \mathbf{y})}{\partial \mathbf{n}_{\mathbf{y}}} (v - u) \right] d\mathbf{s}_{\mathbf{y}}$$

which, by (70) simplifies to give (69) with  $\sigma := (u - v)|_{\gamma}$ . Choosing  $\mathbf{x} \in \partial\Omega$  shows that  $\sigma$  solves (68).

Uniqueness follows by similar arguments as Laplace: instead let  $\sigma$  solve (68) with zero RHS, then let  $u$  be given by (69). Then  $u$  vanishes on  $\partial\Omega$ , so by the uniqueness of the exterior Dirichlet BVP (19)–(21),  $u$  also vanishes throughout  $\mathbb{R}^d \setminus \Omega$ . Since  $u$  is analytic [19, Thm. 2.2], by unique continuation  $u$  also vanishes in  $\mathbb{R}^d \setminus \overline{\Omega_-}$ . By the jump relations its interior limits of  $u$  on  $\gamma$  are  $u^- = -\sigma$  and  $u_{\mathbf{n}}^- = -i\eta\sigma$ . Thus  $u_{\mathbf{n}}^- - i\eta u^- = 0$  on  $\gamma$ , and by construction  $u$  is also a Helmholtz solution in  $\Omega_-$ . By the uniqueness of the impedance BVP in  $\Omega_-$ , then  $u \equiv 0$  in  $\Omega_-$ , so, again by either jump relation,  $\sigma \equiv 0$ .

**Theorem 27 (QFS robustness for exterior Stokes velocity evaluation)** *Let  $(\mathbf{u}, p)$  solve (23)–(24) in  $\Omega \setminus \mathbb{R}^d$ , with  $\mathbf{u} = \mathbf{u}_c$  on  $\partial\Omega$ , and decay condition at infinity  $\mathbf{u}(\mathbf{x}) = \mathbf{\Sigma} \log \|\mathbf{x}\| + o(1)$  in  $d = 2$  or  $\mathbf{u}(\mathbf{x}) = o(1)$  in  $d = 3$  (ie, zero constant term). Let  $(\mathbf{u}, p)$  continue analytically as a Stokes solution throughout the closed annulus (or shell) between  $\partial\Omega$  and a simple smooth interior surface  $\gamma \subset \Omega$ . Let  $d = 3$ , or for  $d = 2$  let the  $2 \times 2$  matrix mapping  $\mathbf{\Sigma}$  to  $\boldsymbol{\omega}$  in (26)*

be nonsingular for both  $\partial\Omega$  and  $\gamma$ . Let  $G$  and  $D$  be as in (27)–(28). Then the (“completed”  $S + D$  representation) first kind integral equation

$$\int_{\gamma} [G(\mathbf{x}, \mathbf{y}) + D(\mathbf{x}, \mathbf{y})] \boldsymbol{\sigma}(\mathbf{y}) d\mathbf{s}_{\mathbf{y}} = \mathbf{u}_c(\mathbf{x}), \quad \mathbf{x} \in \partial\Omega \quad (71)$$

has a unique solution  $\boldsymbol{\sigma} \in C^\infty(\gamma)^d$ , and

$$\mathbf{u}(\mathbf{x}) = \int_{\gamma} [G(\mathbf{x}, \mathbf{y}) + D(\mathbf{x}, \mathbf{y})] \boldsymbol{\sigma}(\mathbf{y}) d\mathbf{s}_{\mathbf{y}}, \quad \mathbf{x} \in \Omega \setminus \mathbb{R}^d. \quad (72)$$

*Proof* The proof is as for Helmholtz but with  $-i\eta$  replaced by 1. The Green’s representation formulae (66)–(67) apply for the Stokes velocity field, with traction data  $\mathbf{T}(\mathbf{u}, p)$  (defined, eg, in [46, Sec. 2.3.1]) in place of normal derivative data, and  $D(\mathbf{x}, \mathbf{y})$  from (28) in place of the scalar kernel  $\partial G(\mathbf{x}, \mathbf{y})/\partial \mathbf{n}_{\mathbf{y}}$ . Then let  $(\mathbf{v}, q)$  solve the homogeneous Stokes BVP interior to  $\gamma$ , with Robin (“impedance”) data

$$\mathbf{T}(\mathbf{v}, q) + \mathbf{v} = \mathbf{T}(\mathbf{u}, p) + \mathbf{u} \quad \text{on } \gamma. \quad (73)$$

A solution exists by Lemma 28 below. Adding (66) (which applies since  $\mathbf{u}$  has a zero constant term), and (67), and adding and subtracting  $\mathbf{v} - \mathbf{u}$ , we get

$$\mathbf{u}(\mathbf{x}) = \int_{\gamma} [G(\mathbf{x}, \mathbf{y}) [\mathbf{T}(\mathbf{v}, q) + \mathbf{v} - (\mathbf{T}(\mathbf{u}, p) + \mathbf{u}) - (\mathbf{v} - \mathbf{u})] - D(\mathbf{x}, \mathbf{y})(\mathbf{v} - \mathbf{u})] d\mathbf{s}_{\mathbf{y}}$$

which, by (73) simplifies to give (72) with  $\boldsymbol{\sigma} := (\mathbf{u} - \mathbf{v})|_{\gamma}$ . Choosing  $\mathbf{x} \in \partial\Omega$  shows that  $\boldsymbol{\sigma}$  solves (71). This completes existence. The uniqueness proof is similar to Laplace, apart from the following. One needs uniqueness for the exterior Stokes Dirichlet BVP with zero constant term: in  $d = 2$  Lemma 2 (logarithmic capacity condition) is replaced by the nonsingularity hypothesis for  $\partial\Omega$  in the theorem statement. The unique continuation argument relies on each component of  $\mathbf{u}$  being analytic [62, p. 60]. The rest of the proof is as for Helmholtz, replacing  $-i\eta$  by 1, with the uniqueness of the interior Robin BVP assured by Lemma 28 below.

**Lemma 28 (Existence and uniqueness for Stokes interior Robin BVP)** *Let  $\Omega \subset \mathbb{R}^d$ , be bounded with smooth boundary  $\partial\Omega$ . Let  $\mathbf{f} : \partial\Omega \rightarrow \mathbb{R}^d$  be given smooth data. Let the vector field  $\mathbf{v}$  and scalar function  $q$  solve in  $\Omega$  the Stokes equations  $-\mu\Delta\mathbf{v} + \nabla q = \mathbf{0}$  and  $\nabla \cdot \mathbf{v} = 0$ , with Robin data  $\mathbf{T}(\mathbf{v}, q) + \mathbf{v} = \mathbf{f}$ . Then this problem has at most one solution. In addition, let  $d = 3$ , or  $d = 2$  and let the  $2 \times 2$  matrix mapping  $\boldsymbol{\Sigma}$  to  $\boldsymbol{\omega}$  in (26) be nonsingular, then it has exactly one solution.*

*Proof* Uniqueness follows easily as in [47, p. 83] [79, p.51]. One uses  $(\mathbf{v}, q)$  for both the solution pairs in Green’s 1st identity [62, p. 53] to get

$$\frac{\mu}{2} \int_{\Omega} \|\nabla \mathbf{v} + \nabla \mathbf{v}^T\|_F^2 = \int_{\partial\Omega} \mathbf{T}(\mathbf{v}, q) \cdot \mathbf{v} ds,$$

where  $F$  indicates the Frobenius norm of the  $d \times d$  tensor. Applying the Robin condition with  $\mathbf{f} \equiv \mathbf{0}$  shows that the right-hand side is non-positive, so that both vanish, so that  $\mathbf{v} \equiv \mathbf{0}$ . For existence, suppose that  $\boldsymbol{\phi} \in C(\partial\Omega)^d$  solves the BIE

$$(S + D^T + 1/2)\boldsymbol{\phi} = \mathbf{f} \quad (74)$$

where  $D^T$  is the adjoint double-layer operator. Then  $\mathbf{v} = S\boldsymbol{\phi}$  solves the Stokes equations in  $\Omega$  with the correct Robin data following from the jump relations, thus is a solution. By the Fredholm alternative, to prove existence for (74), one may prove uniqueness for the adjoint BIE  $(S + D + 1/2)\boldsymbol{\psi} = \mathbf{0}$ . This is already known in  $d = 3$  [40, Thm 2.1]. In  $d = 2$  the constant term again rears its ugly head [47], but given the hypothesis we prove uniqueness as follows. Let  $\boldsymbol{\psi}$  solve the homogeneous adjoint BIE, then construct  $\mathbf{w} = (S + D)\boldsymbol{\psi}$  and  $r$  the corresponding pressure representation, which solve the modified exterior BVP (23)–(26) with given  $\boldsymbol{\omega} = \mathbf{0}$ , but  $\boldsymbol{\Sigma}$  arbitrary. By the  $2 \times 2$  matrix nonsingularity hypothesis the exterior solution is unique, hence trivial. By the jump relations on  $\partial\Omega$ , the interior limits are  $\mathbf{w}^- = \boldsymbol{\psi}$  and  $\mathbf{T}(\mathbf{w}, r)^- = -\boldsymbol{\psi}$ , so that  $(\mathbf{w}, r)$  solves the interior Robin BVP with zero data  $\mathbf{T}(\mathbf{w}, r)^- + \mathbf{w}^- = \mathbf{0}$ . By uniqueness proved above, the solution is identically zero, so again by the jump relations,  $\boldsymbol{\psi} \equiv \mathbf{0}$ .

We suspect that there is a way to remove the above Stokes domain nonsingularity condition in  $d = 2$ , perhaps following [47].

## B Geometry generation for large-scale 2D examples

Here we present an algorithm to generate  $K$  simple polar-Fourier shapes  $\partial\Omega_i$ ,  $i = 1, \dots, K$ , located at randomly-generated centers, that obey the distance and variation criteria of Sec. 4.1. Its inputs are  $d_{\min}$ , a body radius scale  $r_0$ , and a routine `randomcenter` that returns fresh centers  $\mathbf{c}$ .

First we make a list of centers  $\{\mathbf{c}_1, \dots, \mathbf{c}_K\}$  that are far enough apart. Starting with the empty list,

1. Generate a new candidate center  $\mathbf{c}$  via `randomcenter`,
2. Append  $\mathbf{c}$  to the list if  $\mathbf{c}$  has distance at least  $2r_0$  from all  $\mathbf{c}_i$  in the list,
3. Repeat 1-2 until the list has  $K$  centers.

The body  $\partial\Omega_i$  is now chosen from the star-shaped family defined about the center  $\mathbf{c}_i$  by the polar parameterization  $r(t) = r_0(1 + a \cos(ft + \phi))$ , where  $a$  is the “wobble” amplitude,  $f$  its frequency, and  $\phi$  its rotation. For example Figure 1(a) shows  $\mathbf{c} = \mathbf{0}$ ,  $r_0 = 1$ ,  $a = 0.3$ ,  $f = 5$ ,  $\phi = 0.2$ .  $f$  is drawn randomly from  $\{3, 4, \dots, 7\}$  with a distribution function  $\{16/31, 8/31, 4/31, 2/31, 1/31\}$ , to include higher frequencies less often. The amplitude  $a$  is uniform random in  $[0, 0.3(3/f)^{3/2}]$ . Thus higher frequencies will tend to have smaller amplitudes, in order to prevent any single boundary from dominating the resolution requirements.  $\phi$  is uniform random in  $[0, 2\pi)$ . Since the maximum radius of a body is currently  $(1 + a)r_0$ , intersections are possible, and there may not be any bodies that are  $\approx d_{\min}$  apart. Thus we use the following to adjust all body radii:

1. All geometries are rescaled so that the farthest distance from center to boundary is  $r_0 + d_{\min}/2$ . At this point, no boundaries can intersect and all boundaries must be separated by at least  $d_{\min}$ .
2. 10% of the geometries are chosen at random, and for each chosen geometry:
  - (a) Denote the current maximum radius of the geometry by  $R$ .
  - (b) (*expansion*) The geometry is rescaled to increase its radius by  $d_{\min}$ , and minimal separation distances between the geometry and all its nearest neighbors are computed.
  - (c) Step (b) is repeated until either the geometries current radius is  $> 1.5R$ , or the geometry is separated from a nearest neighbor by  $< d_{\min}$ .
  - (d) If the prior step is terminated because the geometry is  $< d_{\min}$  from a nearest neighbor, proceed to the next step; otherwise handling for this geometry is finished.
  - (e) (*rescue*) The geometry is rescaled to decrease its radius by  $d_{\min}/10$ , and separation distances between the geometry and all its nearest neighbors are computed.
  - (f) Step (e) is repeated until the radius of the geometry is between  $(d_{\min}, 1.1d_{\min}]$ .
3. Step 2 is repeated three times.
4. For speed, the prior items are computed using approximate methods (distances are computed pointwise over barely-resolved boundaries), and in rare instances boundaries may be closer together than  $d_{\min}$ . A final *rescue* step is performed for every boundary with upsampled boundaries and using full Newton iterations to compute the minimal distances.

Although elaborate, this process allows us to efficiently place  $K$  polydisperse boundaries in a specified manner throughout a domain, with a separation no less than  $d_{\min}$  between the individual boundaries. When the initial set of boundaries are packed sufficiently tightly, the *expansion* steps always produce at least some boundaries whose expansion is terminated because they are too close to others; thus, due to how the *rescue* stage is implemented, there will always be some close pairs of boundaries separated by between  $d_{\min}$  and  $1.1d_{\min}$ .

## References

1. L. af Klinteberg, T. Askham, and M. C. Kropinski. A fast integral equation method for the two-dimensional navier-stokes equations. *J. Comput. Phys.*, 409:109353, 2020.
2. L. af Klinteberg and A.-K. Tornberg. A fast integral equation method for solid particles in viscous flow using quadrature by expansion. *J. Comput. Phys.*, 326:420–445, 04 2016.
3. B. K. Alpert. Hybrid Gauss-trapezoidal quadrature rules. *SIAM J. Sci. Comput.*, 20:1551–1584, 1999.
4. G. B. Arfken and H. J. Weber. *Mathematical methods for physicists*. Harcourt / Academic Press, 5th edition, 2001.

5. K. Atkinson. *The numerical solution of integral equations of the second kind*. Cambridge University Press, 1997.
6. A. H. Barnett. Evaluation of layer potentials close to the boundary for Laplace and Helmholtz problems on analytic planar domains. *SIAM J. Sci. Comput.*, 36(2):A427–A451, 2014.
7. A. H. Barnett and T. Betcke. Stability and convergence of the Method of Fundamental Solutions for Helmholtz problems on analytic domains. *J. Comput. Phys.*, 227(14):7003–7026, 2008.
8. A. H. Barnett, G. R. Marple, S. Veerapaneni, and L. Zhao. A unified integral equation scheme for doubly-periodic Laplace and Stokes boundary value problems in two dimensions. *Comm. Pure Appl. Math.*, 71(11):2334–80, 2018. [math.na:1611.08038](#).
9. A. H. Barnett, B. Wu, and S. Veerapaneni. Spectrally-accurate quadratures for evaluation of layer potentials close to the boundary for the 2D Stokes and Laplace equations. *SIAM J. Sci. Comput.*, 37(4):B519–B542, 2015.
10. J. Beale and M.-C. Lai. A method for computing nearly singular integrals. *SIAM J. Numer. Anal.*, 38:1902–1925, 2001.
11. G. Biros, L. Ying, and D. Zorin. A fast solver for the stokes equations with distributed forces in complex geometries. *J. Comput. Phys.*, 193(1):317–348, 2004.
12. A. Bogomolny. Fundamental solutions method for elliptic boundary value problems. *SIAM J. Numer. Anal.*, 22(4):644–669, 1985.
13. J. Bremer and Z. Gimbutas. A Nyström method for weakly singular integral operators on surfaces. *J. Comput. Phys.*, 231:4885–4903, 2012.
14. O. P. Bruno and L. A. Kunyansky. Surface scattering in three dimensions: an accelerated high-order solver. *Proc. R. Soc. Lond. A*, 457:2921–2934, 2001.
15. C. Carvalho, S. Khatri, and A. D. Kim. Asymptotic analysis for close evaluation of layer potentials. *J. Comput. Phys.*, 355:327–341, 2018.
16. S. Chaillat, M. Bonnet, and J.-F. Semblat. A multi-level fast multipole BEM for 3-D elastodynamics in the frequency domain. *Computer Methods in Applied Mechanics and Engineering*, 197(49):4233–4249, 2008.
17. H. Cheng, W. Y. Crutchfield, Z. Gimbutas, L. Greengard, F. Ethridge, J. Huang, V. Rokhlin, N. Yarvin, and J. Zhao. A wideband fast multipole method for the Helmholtz equation in three dimensions. *J. Comput. Phys.*, 216:300–325, 2006.
18. W. C. Chew, J. M. Jin, E. Michielssen, and J. Song. *Fast and Efficient Algorithms in Computational Electromagnetics*. Artech House, Boston, MA, 2001.
19. D. Colton and R. Kress. *Inverse acoustic and electromagnetic scattering theory*, volume 93 of *Applied Mathematical Sciences*. Springer-Verlag, Berlin, second edition, 1998.
20. E. Corona, L. Greengard, M. Rachh, and S. Veerapaneni. An integral equation formulation for rigid bodies in Stokes flow in three dimensions. *J. Comput. Phys.*, 332:504–519, 2017.
21. E. Corona and S. Veerapaneni. Boundary integral equation analysis for suspension of spheres in Stokes flow. *J. Comput. Phys.*, 362:327–345, 2018.
22. R. Cortez. The method of regularized stokeslets. *SIAM Journal on Scientific Computing*, 23(4):1204–1225, 2001.
23. P. J. Davis. On the numerical integration of periodic analytic functions. In R. E. Langer, editor, *Proceedings of a Symposium on Numerical Approximations*. University of Wisconsin Press, 1959.
24. P. J. Davis. *The Schwarz function and its applications*. The Mathematical Association of America, Buffalo, N. Y., 1974. The Carus Mathematical Monographs, No. 17.
25. A. Doicu, Y. A. Eremin, and T. Wriedt. *Acoustic and Electromagnetic Scattering Analysis Using Discrete Sources*. Academic Press, San Diego, CA, 2000.
26. F. Fryklund, M. C. A. Kropinski, and A.-K. Tornberg. An integral equation-based numerical method for the forced heat equation on complex domains. *Advances in Computational Mathematics*, 46(5):1–36, 2020.
27. F. Fryklund, E. Lehto, and A.-K. Tornberg. Partition of unity extension of functions on complex domains. *Journal of Computational Physics*, 375:57–79, 2018.
28. M. Ganesh and I. G. Graham. A high-order algorithm for obstacle scattering in three dimensions. *J. Comput. Phys.*, 198:211–424, 2004.
29. A. Gillman and A. Barnett. A fast direct solver for quasiperiodic scattering problems. *J. Comput. Phys.*, 248:309–322, 2013.
30. A. Gillman, A. H. Barnett, and P.-G. Martinsson. A spectrally accurate direct solution technique for frequency-domain scattering problems with variable media. *BIT Numer. Math.*, pages 1–30, 2014.

31. Z. Gimbutas and L. Greengard. FMMLIB2D, Fortran libraries for fast multipole methods in two dimensions, 2012–2021. <https://github.com/zgimbutas/fmmlib2d>.
32. Z. Gimbutas and S. Veerapaneni. A fast algorithm for spherical grid rotations and its application to singular quadrature. *SIAM J. Sci. Comput.*, 5(6):A2738–A2751, 2013.
33. O. Gonzalez. On stable, complete, and singularity-free boundary integral formulations of exterior Stokes flow. *SIAM J. Appl. Math.*, 69(4):933–958, 2009.
34. A. Gopal and L. N. Trefethen. New Laplace and Helmholtz solvers. *Proc. Natl. Acad. Sci. USA*, 116:10223–10225, 2019.
35. L. Greengard and M. Moura. On the numerical evaluation of electrostatic fields in composite materials. *Acta Numerica*, 3:379–410, 1994.
36. L. Greengard, M. O’Neil, M. Rachh, and F. Vico. Fast multipole methods for the evaluation of layer potentials with locally-corrected quadratures. *J. Comput. Phys. X*, 10:100092, 2021.
37. L. Greengard and V. Rokhlin. A fast algorithm for particle simulations. *J. Comput. Phys.*, 73:325–348, 1987.
38. W. Hackbusch. A sparse matrix arithmetic based on H-matrices; Part I: Introduction to H-matrices. *Computing*, 62:89–108, 1999.
39. S. Hao, A. H. Barnett, P. G. Martinsson, and P. Young. High-order accurate Nyström discretization of integral equations with weakly singular kernels on smooth curves in the plane. *Adv. Comput. Math.*, 40(1):245–272, 2014.
40. F.-K. Hebekker. Efficient boundary element methods for three-dimensional exterior viscous flows. *Numer. Methods Partial Differential Equations*, 2:273–297, 1986.
41. J. Helsing. Solving integral equations on piecewise smooth boundaries using the RCIP method: a tutorial, 2017. updated preprint, 51 pages, [arXiv:1207.6737v7](https://arxiv.org/abs/1207.6737v7).
42. J. Helsing and L. Greengard. On the numerical evaluation of elastostatic fields in locally isotropic two-dimensional composites. *J. Mech. Phys. Solids*, 46(8):1441–1462, 1998.
43. J. Helsing and A. Holst. Variants of an explicit kernel-split panel-based Nyström discretization scheme for Helmholtz boundary value problems. *Adv. Comput. Math.*, 41(3):691–708, 2015.
44. J. Helsing and R. Ojala. On the evaluation of layer potentials close to their sources. *J. Comput. Phys.*, 227:2899–2921, 2008.
45. A. Hochman, Y. Leviatan, and J. K. White. On the use of rational-function fitting methods for the solution of 2D Laplace boundary-value problems. *J. Comput. Phys.*, 238:337–358, 2013.
46. G. Hsiao and W. L. Wendland. *Boundary Integral Equations*. Applied Mathematical Sciences, Vol. 164. Springer, 2008.
47. G. C. Hsiao and R. Kress. On an integral equation for the two-dimensional exterior Stokes problem. *App. Numer. Math.*, 1:77–93, 1985.
48. N. I. Ioakimidis, K. E. Papadakis, and E. A. Perdios. Numerical evaluation of analytic functions by Cauchy’s theorem. *BIT Numer. Math.*, 31(2):276–285, 1991.
49. U. Kangro. Convergence of collocation method with delta functions for integral equations of first kind. *Integr. Equ. Oper. Theory*, 66(2):265–282, 2010.
50. U. Kangro. Solution of three-dimensional electromagnetic scattering problems by interior source methods. *AIP Conf. Proc.*, 1479:2328–2331, 2012.
51. S. Kapur and V. Rokhlin. High-order corrected trapezoidal quadrature rules for singular functions. *SIAM J. Numer. Anal.*, 34:1331–1356, 1997.
52. D. Karkashadze. On status of main singularities in 3D scattering problems. In *Proceedings of VIth International Seminar/Workshop on Direct and Inverse Problems of Electromagnetic and Acoustic Wave Theory (DIPED)*, pages 187–190, Lviv, Ukraine, 2001.
53. M. Katsurada. A mathematical study of the charge simulation method. II. *J. Fac. Sci. Univ. Tokyo Sect. IA Math.*, 36(1):135–162, 1989.
54. M. Katsurada. Charge simulation method using exterior mapping functions. *Japan J. Indust. Appl. Math.*, 11(1):47–61, 1994.
55. M. Katsurada and H. Okamoto. The collocation points of the fundamental solution method for the potential problem. *Comput. Math. Appl.*, 31(1):123–137, 1996.
56. A. Klöckner, A. H. Barnett, L. Greengard, and M. O’Neil. Quadrature by expansion: a new method for the evaluation of layer potentials. *J. Comput. Phys.*, 252(1):332–349, 2013.
57. R. Kress. Minimizing the condition number of boundary integral operators in acoustic and electromagnetic scattering. *Quarterly J. Mech. Appl. Math.*, 38:323–341, 1985.



58. R. Kress. Boundary integral equations in time-harmonic acoustic scattering. *Mathl. Comput. Modelling*, 15:229–243, 1991.
59. R. Kress. *Linear Integral Equations*, volume 82 of *Appl. Math. Sci.* Springer, second edition, 1999.
60. S. Krishnan, E. S. Shaqfeh, and G. Iaccarino. Fully resolved viscoelastic particulate simulations using unstructured grids. *Journal of Computational Physics*, 338:313–338, 2017.
61. V. D. Kupradze. On the approximate solution of problems in mathematical physics. *Uspekhi Mat. Nauk*, 22(2(134)):59–107, 1967.
62. O. A. Ladyzhenskaya. *The Mathematical Theory of Viscous Incompressible Flow, revised 2nd edition*. Mathematics and Its Applications 2. Gordon and Breach, 1969.
63. J. Lai, M. Kobayashi, and A. H. Barnett. A fast and robust solver for the scattering from a layered periodic structure containing multi-particle inclusions. *J. Comput. Phys.*, 298:194–208, 2015.
64. J. Lai and M. O’Neil. An FFT-accelerated direct solver for electromagnetic scattering from penetrable axisymmetric objects. *J. Comput. Phys.*, 390:152–174, 2019.
65. N. S. Landkof. *Foundations of modern potential theory*. Springer-Verlag, 1st edition, 1972.
66. C. Li, B. Thomases, and R. D. Guy. Orientation dependent elastic stress concentration at tips of slender objects translating in viscoelastic fluids. *Physical Review Fluids*, 4(3):031301, 2019.
67. Y. Liu and A. H. Barnett. Efficient numerical solution of acoustic scattering from doubly-periodic arrays of axisymmetric objects. *J. Comput. Phys.*, 324:226–245, 2016.
68. Y. L. Liu. *The numerical solution of frequency-domain acoustic and electromagnetic periodic scattering problems*. PhD thesis, Department of Physics, Dartmouth College, 2016. <https://collections.dartmouth.edu/archive/object/dcdis/dcdis-liu2016>.
69. D. Malhotra and G. Biros. PVFMM: A parallel kernel independent FMM for particle and volume potentials. *Commun. Comput. Phys.*, 18(3):808–830, 2015.
70. P.-G. Martinsson. *Fast direct solvers for elliptic PDEs*. SIAM, Philadelphia, 2020.
71. A. Mayo. The fast solution of Poisson’s and the biharmonic equations on irregular regions. *SIAM J. Numer. Anal.*, 21(2):285–299, 1984.
72. M. Morse, A. Rahimian, and D. Zorin. A robust solver for elliptic pdes in 3d complex geometries. *J. Comput. Phys.*, 442:110511, 06 2021.
73. E. Nazockdast, A. Rahimian, D. Needleman, and M. Shelley. Cytoplasmic flows as signatures for the mechanics of mitotic positioning. *Molecular biology of the cell*, 28(23):3261–3270, 2017.
74. E. Nazockdast, A. Rahimian, D. Zorin, and M. Shelley. A fast platform for simulating semi-flexible fiber suspensions applied to cell mechanics. *Journal of Computational Physics*, 329:173–209, 2017.
75. R. G. Owens and T. N. Phillips. Steady viscoelastic flow past a sphere using spectral elements. *International journal for numerical methods in engineering*, 39(9):1517–1534, 1996.
76. C. Pérez-Arancibia, C. Turc, and L. Faria. Planewave density interpolation methods for 3D Helmholtz boundary integral equations. *SIAM J. Sci. Comput.*, 41(4):A2088–A2116, 2019.
77. C. S. Peskin. The immersed boundary method. *Acta numerica*, 11:479–517, 2002.
78. B. Quaife, A. Gannon, and Y.-N. Young. Hydrodynamics of a semipermeable vesicle under flow and confinement. *arXiv preprint arXiv:2102.00140*, 2021.
79. M. Rachh. Integral equation methods for problems in electrostatics, elastostatics and viscous flow, 2015. Ph.D thesis, New York University.
80. M. Rachh and L. Greengard. Integral equation methods for elastance and mobility problems in two dimensions. *SIAM J. Numer. Anal.*, 54(5):2889–2909, 2016.
81. A. Rahimian, A. H. Barnett, and D. Zorin. Ubiquitous evaluation of layer potentials using Quadrature by Kernel-Independent Expansion. *BIT Numer. Math.*, 58:423–456, 2018.
82. V. Rokhlin. Solution of acoustic scattering problems by means of second kind integral equations. *Wave Motion*, 5:257–272, 1983.
83. Y. Saad and M. H. Schultz. GMRES: a generalized minimal residual algorithm for solving nonsymmetric linear systems. *SIAM J. Stat. Sci. Comput.*, 7(3):856–869, 1986.
84. D. Saintillan. Rheology of active fluids. *Annual Review of Fluid Mechanics*, 50:563–592, 2018.

85. A. S. Sangani and G. Mo. Inclusion of lubrication forces in dynamic simulations. *Phys. Fluids*, 6(5):1653–1662, 1994.
86. F.-J. Sayas, T. S. Brown, and M. E. Hassell. *Variational techniques for elliptic partial differential equations: theoretical tools and advanced applications*. CRC Press, Boca Raton, Florida, 2019.
87. F. Shubitidze, H. T. Anastassiou, and D. I. Kaklamani. An improved accuracy version of the method of auxiliary sources for computational electromagnetics. *IEEE Trans. Antennas Propag.*, 52:302–309, 2004.
88. K. Sinha and M. D. Graham. Shape-mediated margination and demargination in flowing multicomponent suspensions of deformable capsules. *Soft matter*, 12(6):1683–1700, 2016.
89. C. Sogrentone, J. I. Kach, A. S. Khair, L. M. Walker, and P. M. Vlahovska. Numerical and asymptotic analysis of the three-dimensional electrohydrodynamic interactions of drop pairs. *Journal of Fluid Mechanics*, 914, 2021.
90. C. Sogrentone and A.-K. Tornberg. A highly accurate boundary integral equation method for surfactant-laden drops in 3D. *J. Comput. Phys.*, 360:167–191, 2018.
91. D. B. Stein, R. D. Guy, and B. Thomases. Convergent solutions of Stokes Oldroyd-B boundary value problems using the immersed boundary smooth extension (IBSE) method. *Journal of Non-Newtonian Fluid Mechanics*, 268:56–65, 2019.
92. M. Theillard, R. Alonso-Matilla, and D. Saintillan. Geometric control of active collective motion. *Soft Matter*, 13(2):363–375, 2017.
93. L. N. Trefethen and J. A. C. Weideman. The exponentially convergent trapezoidal rule. *SIAM Review*, 56(3):385–458, 2014.
94. S. K. Veerapaneni, D. Gueyffier, D. Zorin, and G. Biros. A boundary integral method for simulating the dynamics of inextensible vesicles suspended in a viscous fluid in 2D. *J. Comput. Phys.*, 228(7):2334–2353, 2009.
95. M. Wala and A. Klöckner. A fast algorithm with error bounds for Quadrature by Expansion. *J. Comput. Phys.*, 374:135–162, 2018.
96. J. Wang, E. Nazockdast, and A. Barnett. An integral equation method for the simulation of doubly-periodic suspensions of rigid bodies in a shearing viscous flow. *J. Comput. Phys.*, 424:109809, 2021.
97. B. Wu and P. Martinsson. Zeta correction: a new approach to constructing corrected trapezoidal quadrature rules for singular integral operators. *Adv. Comput. Math.*, 47:45, 2021.
98. B. Wu and P. G. Martinsson. Corrected trapezoidal rules for boundary integral equations in three dimensions, 2020. arxiv:2007.02512.
99. B. Wu, H. Zhu, A. H. Barnett, and S. V. Veerapaneni. Solution of Stokes flow in complex nonsmooth 2D geometries via a linear-scaling high-order adaptive integral equation scheme. *J. Comput. Phys.*, 410:109361, 2020.
100. W. Yan, E. Corona, D. Malhotra, S. Veerapaneni, and M. Shelley. A scalable computational platform for particulate Stokes suspensions. *J. Comput. Phys.*, 416:109524, 2020.
101. L. Ying, G. Biros, and D. Zorin. A high-order 3D boundary integral equation solver for elliptic PDEs in smooth domains. *J. Comput. Phys.*, 216:247–275, 2006.
102. W. Ying and J. T. Beale. A fast accurate boundary integral method for potentials on closely packed cells. *Commun. Comput. Phys.*, 14:1073–1093, 2013.
103. Y.-N. Young, M. J. Shelley, and D. B. Stein. The many behaviors of deformable active droplets. *Mathematical Biosciences and Engineering*, 18(3):2849–2881, 2021.